Sede Amministrativa: Università degli Studi di Padova

Dipartimento di Fisica e Astronomia "G. Galilei"

Corso di Dottorato di Ricerca in Astronomia

Ciclo XXX

Modeling the Extended narrow line Region

In the era of Integral-Field surveys

Coordinatore: Ch.mo Prof. Giampaolo Piotto

Supervisore: Dr. Stefano Ciroi

Co-Supervisore: Dr. Francesco Di Mille

ii

<div align="right">**Dottorando:** Michele Frezzato</div>

The truth will set you free. But not until it is finished with you.

David Foster Wallace - Infinite Jest

iv

Contents

Abstract

The Extended Narrow Line Region (ENLR) of Active Galactic Nuclei (AGN) is a region of highly ionized gas with conical or bi-conical shape, extending from the Narrow Line Region ($\sim$ 100 pc) up to 15-20 kpc with the apexes pointing towards the nucleus. At the moment ~ 50 galaxies have been found showing evidence of ENLR, the vast majority of which are nearby Seyfert galaxies. The presence of these cones is interpreted in the framework of the Unified Model of AGN that predicts an anisotropic radiation field escaping from the nucleus, collimated by a dusty torus. The strong non-thermal radiation produced by the accretion disk seems indeed to be the main responsible of the ionization in the ENLR, although the contribution of shocks cannot always be neglected. The ionized gas however does not reside entirely inside the cones. There is evidence of several Seyfert galaxies (e.g. NGC 4151, Mrk 3, NGC 3393) showing low-ionization lines emission, identifiable in BPT diagnostic diagrams as LINERs emission, located in the outskirts of the cones or even in the cross-cone region. It is argued that these spatial variation of the ionization in the ENLR may be a new channel in the study of the collimation by the torus and could provide valuable information on the torus structure (e.g. clumpiness, edge features). Moreover, recent advances in integral field spectroscopy and the start of the first integral field survey could provide an unprecedented advantage in a more thorough characterization of this phenomenon.

The theoretical study of ionized gas in AGN is mainly carried out through photo-ionization models realized with dedicated codes. The radiative transfer, ionization and chemistry calculations are solved numerically due to the complexity of the problem. The state of the art of these models still relies on an ad hoc single-zone or two-zone approach, able to reproduce the gas spectral features in detail,

however not suited to study spatial effects in the ENLR.

The aim of this work is to explore a new method to realize photo-ionization models of ENLR, taking into account both a cloud-based distributions of gas and the effects of the torus structure on the collimation of the nuclear radiation and on the ionization of gas inside and outside the cones. For the first time the models will be bi-dimensional in order to provide a useful tool to be compared with integral field data.

To achieve this goal we developed a PYTHON code able to perform a procedural generation of the gas distribution in different regions of space, i.e. the cloud parameters as their position, dimension and mass are randomly drawn from a probability distribution determined by the user. This multi-cloud approach is intended to avoid the simple assumption typical of traditional photo-ionization models and at the same time to reproduce the observation with a more realistic ansatz on the distribution of gas. The user can, for instance, generate clouds of gas in the galactic disk and ionize them with a chosen Spectral Energy Distribution (SED). To collimate the radiation we included a simple torus model, either clumpy, smooth or composite. The code interfaces with *Cloudy*, the photo-ionization code, through the pyCloudy libraries, and it is able to define a set of models, write the input files and, after the calculations are over, read and plot the results.

Chapter 1

Introduction

"Quasars are the fire-breathing bat-winged vampire rainbow zebra unicorns of astrophysical phenomena!"

PBS Spacetime - Why quasars are so awesome

In this chapter we introduce the subject and the scientific rationale of this PhD thesis. In section 1.1 we will briefly review Active Galactic Nuclei (AGN) and Seyfert galaxies, and their emitting regions. In section 1.2 we will focus on the Extended Narrow Line Region (ENLR) while in section 1.3 we discuss the AGN obscuration and the collimation of the ENLR. Section 1.4 is dedicated to summarize the state of the art of ENLR models and in section 1.5 we will see how integral field spectroscopy may impact on the study of the ENLR in AGN. Finally in section 1.6 we will explain the aim of this PhD thesis.

1.1 Active Galactic Nuclei

Active Galactic Nuclei is a common designation of a vast zoology of celestial objects (see table 1.1 for a complete taxonomy). They are powerful and compact energy sources located in the nuclei of galaxies, characterized by very high

luminosity across all the electromagnetic spectrum: their emission covers radio, infrared, optical, ultraviolet, X-ray and sometimes γ-ray bands. This electromagnetic emission cannot be attributed to stars but instead it is associated with gas accretion on a supermassive black hole (SMBH) located in the center of the host galaxy. This consideration rises from the luminosity and compactness of the emitting region and its non-thermal spectrum, ruling out the contribution of stars. The AGN class includes objects with luminosity spanning over a wide range, from $L_{\mathrm{AGN}} \sim 10^{41}\,\mathrm{erg\,s^{-1}}$ in the case of LINERs (Low-Ionization Nuclear Emitting Line Regions) up to $L_{\mathrm{AGN}} \sim 10^{47}\,\mathrm{erg\,s^{-1}}$ in bright quasars.

The SMBH ($10^5 M_\odot \lesssim M_{\mathrm{BH}} \lesssim 10^{10} M_\odot$) is expected to accrete with Eddington ratio $L_{\mathrm{AGN}}/L_{\mathrm{EDD}} > 10^{-5}$ (Netzer, 2015), where L_{AGN} is the bolometric luminosity and $L_{\mathrm{EDD}} = 1.26 \times 10^{38} M_{\mathrm{BH}}/M_\odot\,\mathrm{erg\,s^{-1}}$ is the Eddington luminosity for a solar composition gas. However aside from these common features AGN share other characteristics: the accretion is usually a sub-pc rotationally dominated flow, in the form of a geometrically thin (or thick) accretion disk; the high density gas in Keplerian motion around the BH is referred to as the Broad Line Region (BLR, see 1.1.1); the lower density gas located further away from the BH and moving slower with respect to the BLR, is the Narrow Line Region; around the accretion disk and the BLR there is the torus, a dusty axisymmetric structure providing partial occultation of the nucleus; occasionally a radio jet is associated with radio and γ-ray emission.

Given the large number of different properties, the AGN classification led to a considerable amount of designations and acronyms. Organizing them in a coherent unification scheme has proven to be a challenging task and many possible solutions have been proposed over the years. The principal subdivision is based on the $R = F_{5GHz}/F_B$ flux ratio, with the rather arbitrary threshold $R = 10$, separating radio-loud AGN ($R > 10$) from radio-quiet (Urry & Padovani, 1995). Among radio-quiet objects are Seyfert galaxies (type I and II), QSO and LINERs while Quasars, Radio Galaxies (BLRG, NLRG, FR1, FR2) and Blazars are radio-loud. From this limited selection of classifications is evident why the idea of a unification scheme, explaining with a small set of physical parameters the large diversity of observed AGN, is appealing.

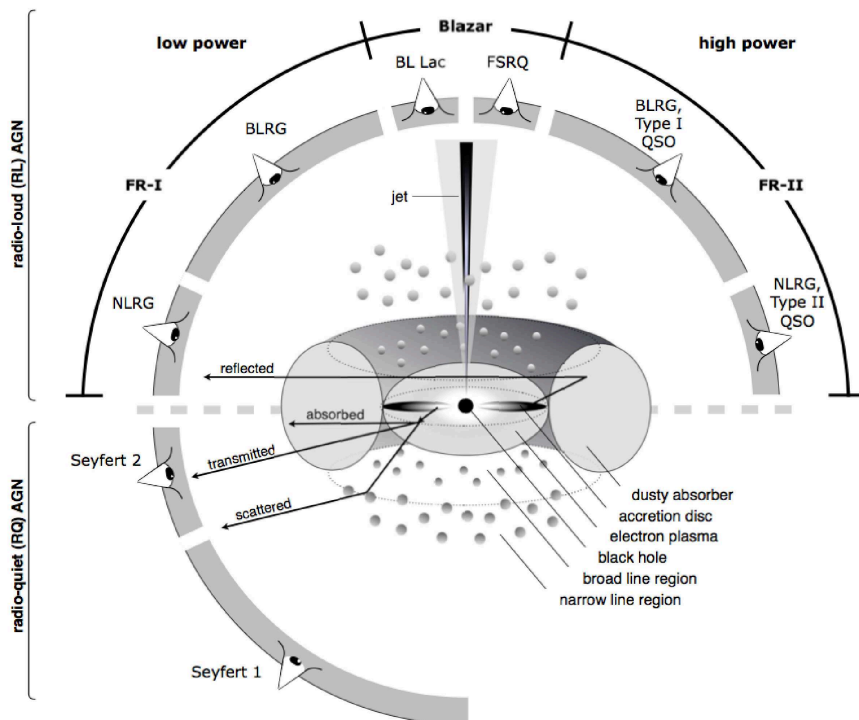The most famous Unified Model was developed by Antonucci (1993) following

Figure 1.1: Schematic representation of the Unified Model (Beckmann & Shrader, 2012). The type of object depends on the viewing angle, on the AGN power and on the presence or absence of a relativistic jet.

the observation of the hidden BLR of NGC 1068 in polarized light (Antonucci &
Miller, 1985). NGC 1068 is a prototype Seyfert 2 galaxy, showing in its spectrum
only the NLR. The discovery of an hidden BLR whose light is reflected and po-
larized in the NLR led to the formulation of the Unified Model. The underlying
idea is that the differences between type 1 and type 2 objects are ultimately a
projection effect and can be explained in terms of inclination of the line of sight
with respect to the AGN itself (see figure 1.1). This is possible because AGN
are anisotropic emitters due to the presence of a dusty obscurer, the torus (see
section 1.3). This simple scheme has been challenged in many ways, for instance
does not account for the radio-loud/radio-quit dichotomy or does not really ex-
plain the presence of "real type-II" AGN which do not show the hidden BLR and
show little X-ray absorption (Panessa & Bassani, 2002; Tran, 2003; Shi et al.,
2010; Marinucci et al., 2012). The general framework however still holds and
many implications have been confirmed over the years, like the presence of the
torus whose emission is observed in the IR and its dimension estimated by dust
reverberation mapping techniques, and ionization cones whose collimation can
be explained in first approximation by the torus itself.
Now we focus on Seyfert galaxies and their optical emission.

1.1.1   Seyfert galaxies and their emission line regions

Seyfert galaxies are the first identified AGN and their discovery dates back
to 1943, when Seyfert observed redshifted emission lines in galaxies. The
distance of these objects implied high luminosity, hence a different and powerful
mechanism of emission. Nowadays Seyfert galaxies are the most common AGN
in the local universe and thanks to their proximity we are able to study in
detail the processes at work in their nucleus. Their identification is based on
the nuclear spectral signatures at optical wavelengths. In case highly ionized
emission lines are present, the galaxy may classify as a Seyfert. The AGN
however is not the only possible ionization mechanism in galaxies: emission lines
are often produced by massive gas clouds of ionized hydrogen, H II regions where
star formation takes place and can contaminate the spectrum. To discriminate
between the two mechanisms (or three when including shocks), Baldwin et al.

Class/Acronym	Meaning	Main properties/reference
Quasar	Quasi-stellar radio source (originally)	Radio detection no longer required
Sey1	Seyfert 1	FWHM $\gtrsim 1000\,km\,s^{-1}$
Sey2	Seyfert 2	FWHM $\lesssim 1000\,km\,s^{-1}$
QSO	Quasi-stellar object	Quasar-like, non-radio source
QSO	Quasi-stellar object 2	High power Sey2
RQ AGN	Radio-quiet AGN	Padovani 2016
RL AGN	Radio-loud AGN	Padovani 2016
Jetted AGN		with strong relativistic jets
Non-jetted AGN		without strong relativistic jets
Type 1		Sey1 and quasars
Type 2		Sey2 and QSO2
FR I	Faranoff-Riley class I	Fanaroff & Riley 1974
FR II	Faranoff-Riley class II	Fanaroff & Riley 1974
BL Lac	BL Lacertae object	Giommi et al. 2012
Blazar	BL Lac and quasar	BL Lacs and FSRQs
BAL	Broad absorption line (quasar)	Weymann et al. 1981
BLO	Broad line object	FWHM $\gtrsim 1000\,km\,s^{-1}$
BLAGN	Broad line AGN	FWHM $\lesssim 1000\,km\,s^{-1}$
BLRG	Broad line radio galaxy	RL Sey1
CDQ	Core-dominated quasar	RL AGN, $f_{core} \geq f_{ext}$ (same as FSRQ)
CSS	Compact steep spectrum radio source	core dominated, $\alpha_r > 0.5$
CT	Compton-thick	$N_H > 1.5 \times 10^{24}\,cm^{-2}$
FR 0	Fanaroff-Riley class 0 radio source	Ghiselini 2010
FSRQ	Flat-spectrum radio quasar	RL AGN, $\alpha_r \leq 0.5$
GPS	Gigahertz-peaked radio source	O'Dea et al. 1991
HBL/HSP	High-energy cutoff BL Lac/blazar	$\nu_{peak} \geq 10^{15}\,Hz$ Padovani & Giommi 1995
HEG	High-excitation galaxy	Laing et al. 1994
HPQ	High polarization quasar	$P_{opt} \geq 3\%$ (same as FSRQ)
Jet-mode		$L_{kin} \gg L_{rad}$ (same as LERG); Heckman & Best 2014
IBL/ISP	Intermediate-energy cutoff BL Lac/blazar	$10^{14} \leq \nu_{peak} \leq 10^{15}\,Hz$ Padovani & Giommi 1995
LINER	Low-ionization nuclear emission-line regions	Heckman & Best 2014
LLAGN	Low-luminosity AGN	Ho 2008
LBL/LSP	Low-energy cutoff BL Lac/blazar	$\nu_{synchpeak} < 10^{14}\,Hz$ Padovani & Giommi 1995
LDQ	Lobe-dominated quasar	RL AGN, $f_{core} < f_{ext}$
LEG	Low-excitation galaxy	Laing et al. 1994
LPQ	Low polarization quasar	$P_{opt} < 3\%$
NLAGN	narrow line AGN	FWHM $\lesssim 1000\,kms^{-1}$
NLRG	narrow line radio galaxy	RL Sey2
NLS1	narrow line Seyfert 1	Osterbrock & Pogge 1985
OVV	Optically violently variable (quasar)	(same as FSRQ)
Population A		Sulentic et al. 2002
Population B		Sulentic et al. 2002
Radiative-mode		Seyferts and quasars; Heckman & Best 2014
RBL	Radio-selected BL Lac BL Lac selected in the radio band	
Sey1.5	Seyfert 1.5	Osterbrock 1981
Sey1.8	Seyfert 1.8	Osterbrock 1981
Sey1.9	Seyfert 1.9	Osterbrock 1981
SSRQ	Steep-spectrum radio quasar	RL AGN, $\alpha_r > 0.5$
USS	Ultra-steep spectrum source	RL AGN, $\alpha_r > 1.0$
XBL	X-ray-selected BL Lac	BL Lac selected in the X-ray band
XBONG	X-ray bright optically normal galaxy	AGN only in the X-ray band/weak lined AGN

Table 1.1: The AGN zoo. Table from Padovani et al. (2017). The top part of the table refers to canonical classes.

(1981) and Veilleux & Osterbrock (1987) developed the line ratios diagnostic diagrams. Since different sources of ionization produce different line ratios in the gas, comparing two or more BPT-VO diagrams it is possible to safely identify the ionization source (see figure 1.2 for details).

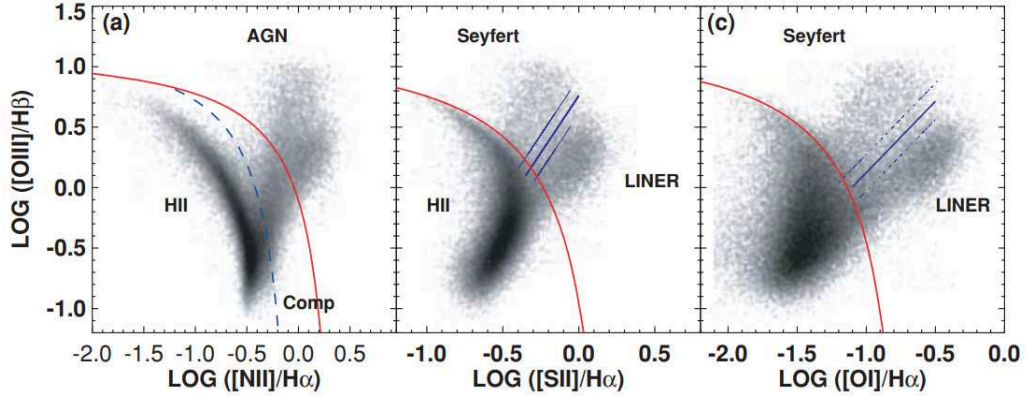The first separation in the Seyfert class was made in accordance with the

Figure 1.2: BPT diagrams from Kewley et al. (2006). Red solid line is the boundary of extreme starburst (Kewley et al., 2001). The blue dashed line is the pure star forming line (Kauffmann et al., 2003). The blue solid line separates Seyfert galaxies from LINERs (Kewley et al., 2006).

relative width of narrow forbidden lines (e.g. [O II]λ3727, [O III]λ5007, [N II]λ6584, [Ne III]λ3869 and [S II]$\lambda\lambda$6717 6731) and the Balmer lines (mainly H$_\alpha$, H$_\beta$ and H$_\gamma$). In Seyfert 1 class the Balmer lines appear broader than the forbidden ones while in Seyfert 2 the width is comparable.

This difference is interpreted as the emission of different regions of gas: the narrow lines originate in a low-density gas with typical electron densities of $n_e \simeq 10^3 - 10^6 \, cm^{-3}$ and typical velocities of hundreds of kilometers per second. Conversely the broad Balmer lines originate from dense matter with $n_e \geq 10^9 \, cm^{-3}$ and the line widths indicate velocities of $10^3 - 10^4 \, km\,s^{-1}$ (Beckmann & Shrader, 2012).

Broad line and narrow line regions

The two regions of gas are believed to be located in different positions in the AGN. This consideration arises basically from two elements: the velocities inferred from line widths, and the (apparent) absence of Broad line Region (BLR) in type 2 objects.

The physical properties of the BLR have been determined on the basis of photo-ionization models, assuming the clouds to be in photo-ionization equilibrium, i.e

the rate of photo-ionization balances the rate of recombination. In a plasma satisfying this condition, observing different ionization states of the same element, it is possible to determine physical parameters, among which the gas temperature and density. For the BLR typical temperature are around $T_{BLR} \sim 10^4 \, \mathrm{K}$, with electron densities $n_e \sim 10^9 \, cm^{-3}$. These temperatures can be responsible of a thermal line broadening of order $10 \, \mathrm{km \, s^{-1}}$, but the BLR gas is moving with high velocities and a plausible explanation is that it is close to a central compact object. Conversely NLR gas shows much slower motions, therefore it cannot be at the same distance from the BH.

These considerations are in agreement with the Unified Model: both the BLR and the NLR are visible in type 1 objects because the observer sees the torus face-on, meaning that the line of sight is pointed towards the central engine where the BLR is located. In type 2 objects instead only the NLR is visible because the BLR is obscured by the torus (see figure 1.1).

The Seyfert classification was later improved introducing the intermediate types 1.5, 1.8, 1.9 (Osterbrock, 1981). These objects show composite line profiles with both broad and narrow component. The number in the classification represents the relative weight of the broad component, gradually disappearing towards type 2.

Another subset of Seyfert galaxies worth mentioning are Narrow line Seyfert 1 galaxies (NLS1), firstly designed as a new subclass by Osterbrock & Pogge in 1985. By definition these AGN have a relatively low full width half maximum (FWHM) of the permitted lines, specifically $\mathrm{FWHM(H_\beta)} < 2000 \, \mathrm{km \, s^{-1}}$ and a $\mathrm{[OIII]/H_\beta}$ flux ratio lower than 3 (Osterbrock & Pogge, 1987; Goodrich, 1989). The presence of strong Fe II multiplets in the spectrum means that the BLR is directly visible. The narrowness of permitted lines is not due to obscuration but instead it is interpreted as due to low rotational velocity of the BLR clouds around a relatively low mass BH ($M_{\mathrm{BH}} \sim 10^{6-8} \, M_\odot$, Mathur (2000)). The low M_{BH} along with the high Eddington ratio (Boroson & Green, 1992) is sometimes interpreted as consequence of the young age of these sources (Grupe, 2000; Mathur, 2000).
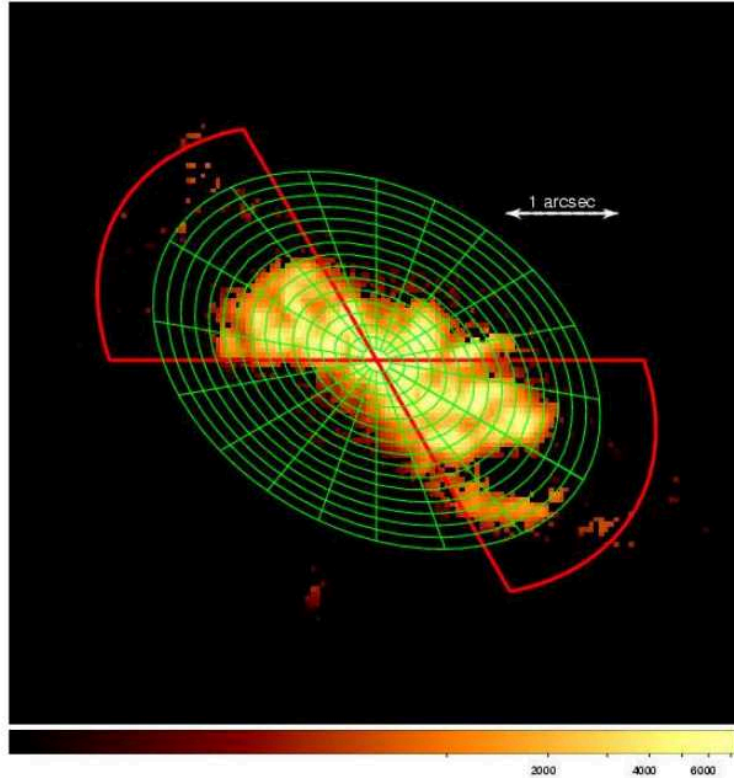
Figure 1.3: Continuum subtracted [O III] image of NGC 4151. On the ENLR it is superimposed the reconstructed orientation of the ionization cones (in red) and the galactic disk (in green) (Kraemer et al., 2008).

1.2   The Extended Narrow Line Region

While the BLR resides close to the SMBH, within the sublimation radius of the dusty torus, the NLR can extend far beyond the nucleus. Numerous imaging survey carried out in the last thirty years through broad-band (UBVR) and narrow-band interference filters ([O III] and H_α) revealed elongated structures of emitting gas with conical or even bi-conical shape in a handful of Seyfert 2 and intermediate Seyfert galaxies (see e.g. Pogge 1988; Tadhunter & Tsvetanov 1989; Mulchaey et al. 1996; Schmitt et al. 2003). These structures have been named ionization cones or extended narrow line region (ENLR), being in all respects a natural extension of the NLR itself. The presence of one-sided cones is easily understandable: given the large amount of obscuring material that might be present in the host galaxy, only the side of the cone emerging towards the

observer from the host galaxy should be visible (Pogge, 1989).

Until now the number of sources with detected ENLR is around 50 (Netzer, 2015), mainly found in type 2 objects with some notable exceptions. In the simplest picture, assuming the cones result from the shadowing of the torus, ionization cones are not expected in type 1 objects because the line of sight would fall within the cone. However there is evidence of ionization cones in a few intermediate type Seyfert 1.5, one notable case being NGC 4151 (Evans et al., 1993) as can be seen in figure 1.3, and other examples are NGC 4253 (Mulchaey et al., 1996), Mrk 6 (Meaburn et al., 1989) and NGC 3783 (Müller-Sánchez et al., 2011). A possible explanation proposed for NGC 4151 is that the observer line of sight crosses a lower density atmosphere on the edge of the torus, with a column density of $10^{20} - 10^{21} \, cm^{-2}$, sufficient to be optically thick to all wavelengths between the Lyman edge and soft X-rays (Evans et al., 1993; Tsvetanov et al., 1996). The atmosphere would be able to collimate the ionizing radiation and still let the BLR visible. The triangular morphology of the cones intersecting a disk-shaped gas distribution would still be visible, under certain conditions in the disk and torus orientation, even if the line of sight lies within the cone (Robinson et al., 1994).

Another puzzling example is Mrk 783, a NLS1 with a detected kiloparsec radio emission (Congiu et al., 2017a) that revealed a huge extended emission region of $\sim 35 \, kpc$, the largest one detected in the local universe so far (Congiu et al. 2017b, submitted).

The most complete information we can get from the observation of the ENLR comes from integral field spectroscopy (IFS, see section 1.5). This technique combines the spectra of the target with the spatial information, providing locally details about the gas ionization and kinematics. At the present the number of ENLR observed with IFS is still limited (~ 25) however this number is destined to increase in the next years.

Kinematics can help to shed light on another open problem in the study of ENLR: the origin of the gas and perhaps why the ENLR is observed only in a small fraction of active galaxies. This very small number may be caused by a selection effect, since it is visible only in nearby galaxies, with a few notable exceptions (Kreimeyer & Veilleux, 2013). Another possible cause is that usually
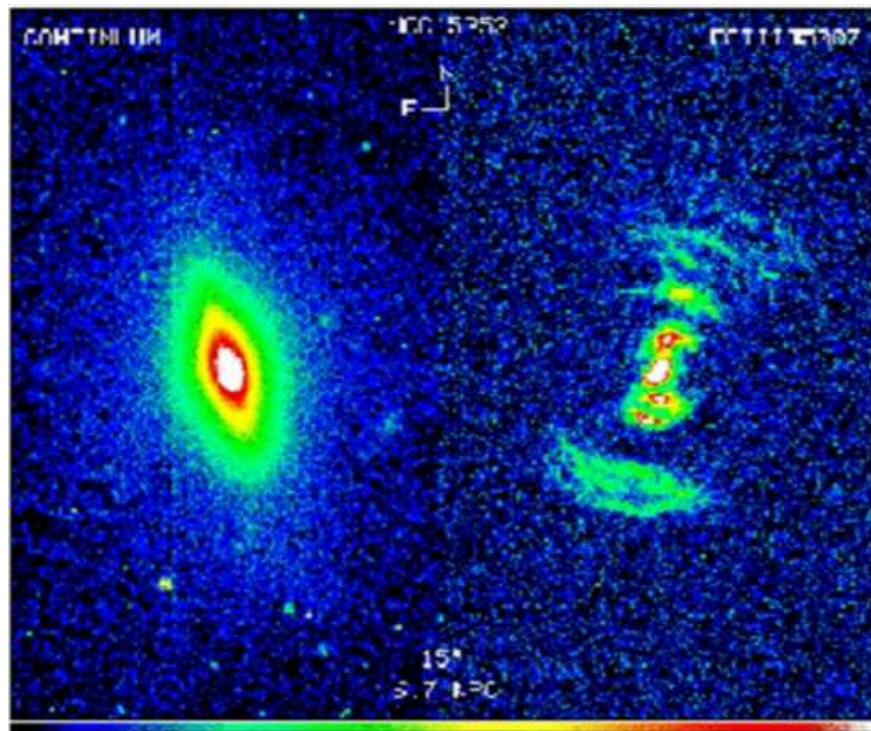
Figure 1.4: The extended narrow line region of NGC 5252 (Tadhunter & Tsve-tanov, 1989). On the left the continuum emission is shown. On the right it is presented the narrow-band interference [O III] filter imaging where the biconical ENLR is visible.

active galaxies lack large scale inter-stellar medium (ISM) so their NLR has a small extension and appears point-like in observations. The presence of gas may then be linked to merger events with gas rich galaxies.

The first observations (Unger et al., 1987) found that the emission in the ENLR was highly elongated, with extremely narrow lines. This slowly varying velocity field suggested the gas was undergoing ordinary galactic rotation and was then part of the galactic disk. Over the years, however, this picture was complicated by other observations. For instance, in the case of NGC 5252 (see figure 1.4) Morse et al. (1998) argued that the formation of ionization cones was likely the consequence of a merger with a dwarf galaxy whose gas was stripped by tidal forces. Mergers seem to be the case of Mrk 3 (Di Mille, PhD thesis 2007), NGC 4388 (Yoshida et al., 2002; Ciroi et al., 2003), Mrk 315 (Ciroi et al., 2005) and NGC 7212 (Cracco et al., 2011). Another possibility is that the gas is expelled by the AGN itself in powerful winds or outflows. Fischer et al. (2013) found clear signatures of bi-conical outflows in a sample of 17 AGN. Curiously the inferred inclination of the NLR showed no correlation with the inclination of the host galaxy disk.

1.2.1 Collimation

The presence of an axisymmetric obscurer with a central opening is a good explanation for these peculiar features, leaving a free two-sided conical "escape route" for ionizing photons. However, several other explanations for the collimation have been proposed. We briefly describe them for completeness. Madau (1988) proposed an intrinsic model of collimation, advocating the presence of a thick accretion disk supported by radiation pressure. The role of the thick accretion disk is similar to the torus, absorbing ionizing photons at large separation angles from the disk axis. Another proposed collimation mechanism is a blazar-like beam produced by a relativistic jet (Tadhunter et al., 1988). The idea is appealing because the ENLR axis if often coincident with the radio axis of the AGN. However the relativistic beaming is dependent on the separation angle from the jet axis and should produce a smooth azimuthal variation of the ionization in the cones. Jets are an important component in the ENLR kinematics and are

likely responsible of shock production, however they do not seem to play a major role in the collimation. The collimation from the torus remains then the most likely explanation; in section 1.3.1 we will review the possible impact of torus clumpiness on the ENLR.

1.3   The torus

After the initial hypothesis linking the spectral differences of Seyfert galaxies (Antonucci & Miller, 1985) to the presence of obscuring material, covering a finite solid angle around the source of radiation, the scientific consensus formed around the torus model. The name refers to the geometrical torus, a surface of revolution obtained by revolving a circle in three dimensional space about an axis coplanar with the circle, due to the idea that this obscurator should have a "doughnut" shape, a ring of dust and gas surrounding and feeding the AGN (Krolik & Begelman, 1988).

With the term "torus" or "central torus" we refer to the structure that extends beyond the dust sublimation radius, before which the inner accretion disk lies. It is clear that the two must be linked by some mechanism allowing the gas to lose angular momentum and feed the AGN, and probably the transition between disk and torus happens without discontinuities. This connection is still unclear and beyond the scope of this work, we refer the interested reader to Krolik & Begelman (1988); Collin & Zahn (1999); Emmering et al. (1992); Schartmann et al. (2005); Collin & Zahn (2008); Beckert & Duschl (2004); Hönig & Beckert (2007); Krolik (2007); Elitzur & Shlosman (2006); Vollmer et al. (2008); Wada et al. (2009a,b); Schartmann et al. (2010) for a panoramic tour of theoretical models of tori and accretion disks.

Another approach to model the torus is phenomenological. We refer to ad hoc models realized to better describe observations and reproduce the emitted SED, these can be basically subdivided into three types: smooth, clumpy and composite. The firsts are continuous gas and dust distributions (e.g. Pier & Krolik 1992; Granato et al. 1997; Fritz et al. 2006) where the dust temperature decreases monotonically as a function of the distance from the BH. Clumpy models are based on the idea that the dust is concentrated in clumps,

surrounded by free space (Nenkova et al., 2008a,b; Hönig & Kishimoto, 2010). This allows a large spread in temperatures inside the torus because a clump beyond the sublimation radius (r_{sub}) can receive un-attenuated radiation. The other consequence is that free space may in principle allow a free line of sight to the center of the AGN (see section 1.3.1). The third way fuses the two previous approaches: the void between the clumps are filled with diluted gas which absorbs part of the incident radiation (Stalevski et al., 2012) and it is perhaps a more realistic picture.

1.3.1 Shape and boundaries

As we anticipated before we refer to the torus as the structure that lies beyond the dust sublimation radius, becoming the inner boundary. However the definition of the sublimation radius itself is tricky. The sublimation distance depends on the grain size and composition and the local radiation flux. The maximum sublimation temperature is different for silicate and graphite grains, being respectively $T_{sub} = 1800K$ and $T_{sub} = 1400K$. Considering the distribution of ISM-type grain sizes and averaging over it, a mean sublimation radius can be defined (Barvainis, 1987):

$$\langle R_{sub,C} \rangle \simeq 0.5 L_{46}^{\frac{1}{2}} \left[\frac{1800}{T_{sub}} \right]^{2.6} f(\theta) \, pc \qquad (1.1)$$

$$\langle R_{sub,Si} \rangle \simeq 1.3 L_{46}^{\frac{1}{2}} \left[\frac{1500}{T_{sub}} \right]^{2.6} f(\theta) \, pc \qquad (1.2)$$

where $L_{46} = L_{tot}/10^{46} \, erg \, s^{-1}$ is the AGN luminosity and $f(\theta)$ is a term which takes into account an anisotropic component of the source. Equations (1.1) and (1.2) are computed for an average grain size of $0.05 \, \mu m$. An reasonable approximation can be achieve through reverberation mapping measurements (RM). The underlying idea is that variable luminosity of the central source stimulates time-dependent heating and ionization of gas and dust in the proximity and that this time-lag can be used to estimate the distances involved. This technique has been widely used to map the distribution of gas in the BLR (see e.g. Kaspi et al.

2000; Bentz et al. 2013), but also to measure time-dependent dust emission in the NIR K-band (see e.g. Glass 1992; Suganuma et al. 2006; Koshida et al. 2014). The response of K-band is a good indicator of the inner boundary because its wavelength ($\sim 2.2\,\mu m$) is close to the peak emissivity of the hottest dust. To an acceptable degree of approximation then $R_{2.2\mu m} = \langle R_{sub,C} \rangle$.

For what concerns the outer torus boundary, the general picture does not require a sharp edge but rather a gradual dilution of the gas and dust into the ISM. It is assumed in theoretical models that the outer radius should be $R_{out} \sim 20 - 170\ R_{sub}$ (Siebenmorgen et al., 2015), while from medium infrared observations the inferred size is approximately less than 10 pc (Tristram et al., 2009; Burtscher et al., 2013).

There is not yet consensus on the mechanism providing vertical stability to the torus. Possible mechanisms are turbulent or outflow motion (Beckert & Duschl, 2004), optical, UV and IR radiation pressure (e.g. Hönig & Beckert 2007), magnetic winds (Emmering et al., 1992) or star formation in the infalling gas. All of the above mechanisms were included in the three-dimensional hydrodynamic simulation of Wada et al. (2009a) and Wada et al. (2009b).
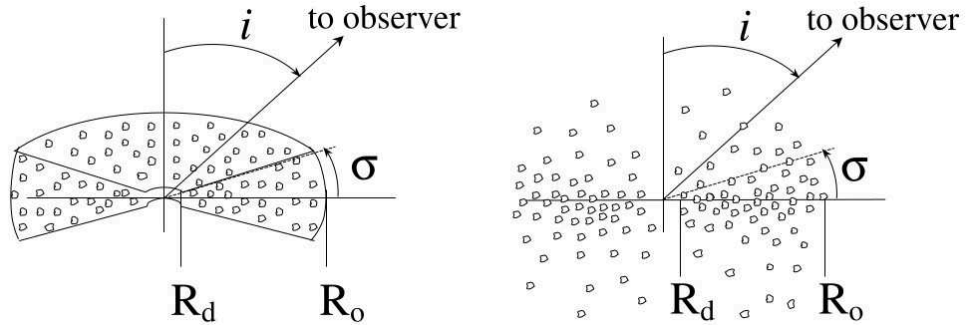

Figure 1.5: Visual representation of the clumpy torus model from Nenkova et al. (2008b)

.

Clumpiness

The idea that the torus may be composed of several clumps of gas and dust (see fig. 1.5) followed shortly the discovery of the hidden BLR in NGC 1068 (Krolik & Begelman, 1986, 1988). Over the years this hypothesis collected a

considerable amount of evidence, from VLTI interferometric observations (Tristram et al., 2007) to the detection of variable X-ray flux in Mrk 3, a Seyfert 2 galaxy (Guainazzi et al., 2016). The clumpy torus model right now represents a widely accepted picture and it is the best choice when trying to reproduce the observed NIR and MIR SED of the torus (Mor et al., 2009; Nenkova et al., 2008b; Siebenmorgen et al., 2015).

Ionizing radiation leaking from gaps in the clumps composing the torus may well be responsible for the ionization of gas in regions outside the ionization cones as pointed out by Kraemer et al. (2008) for NGC 4151. A similar example is the case of NGC 3393, where LINER-like ionization is detected in the cross-cone region (Maksym et al., 2016) (see figure 1.6) .

1.4 Photo-ionization models in the literature

The photo-ionization of gas involves many different processes and building a model able to reproduce the observed spectral features is indisputably a taxing challenge. As reviewed by Netzer (2008) there are five fundamental processes regulating the emissions of the ionized gas in AGN: the photo-ionization and radiative recombination, the thermal balance, the ionizing spectrum, the gas composition and clouds distribution and kinematics. Each one of these is only a macro-category and involves many other subprocesses. For instance, the first one involves dielectronic recombination, Auger ionization, heating and ionization by secondary electrons, charge exchange, collisional ionization, three body recombination and Compton ionization, heating and cooling. In thermal balance must be included dust, that cannot be neglected in the NLR. All these processes are usually treated by dedicated photo-ionization codes that are used to solve numerically the ionization and thermal structure of a single gas cloud.

Because of this intrinsic complexity the first attempts to study the BLR and the NLR of AGN relied on single-zone models.
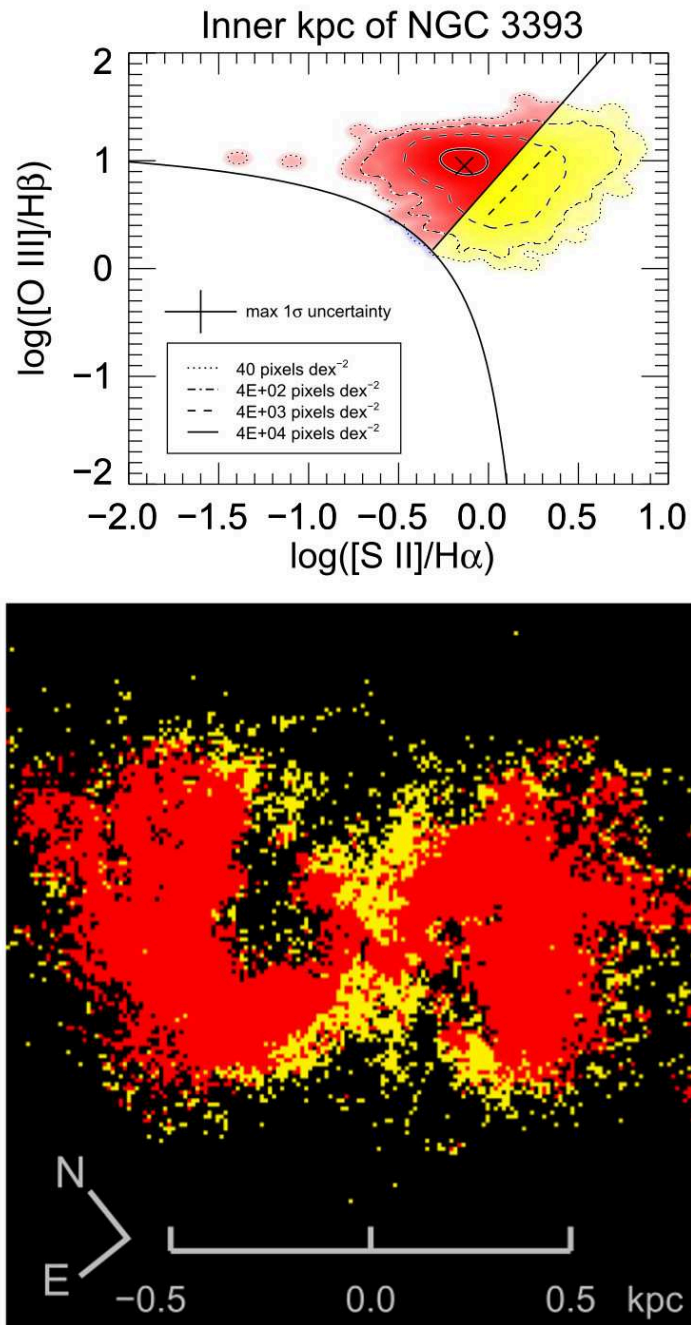
Figure 1.6: Resolved BPT image of NGC 3393 from Maksym et al. (2016). In the top panel it is possible to see the position in the BPT diagram of the pixels of HST WFC3 image of NCG 3393 obtained with narrow-band filters. Red and yellow dots are separated by the Seyfert-LINERs separation line as defined by Kewley et al. (2006). In the bottom panel the image is reconstructed on the basis of the pixel position in the BPT diagram. We can see how the cone edges andthe cross-cone region are identified as LINER emission, i.e. low-ionization regions not caused by star formation.

1.4.1 Single-zone models

Single-zone models (e.g. Stasińska 1984) reproduce the ionization of a single, ionization-bounded, gas cloud of hydrogen with number density n_H caused by a continuum source. It is useful to define the ionization parameter (see Osterbrock & Ferland 2006):

$$U = \frac{1}{4\pi R^2 c\, n_H} \int_{\nu_0}^{\infty} \frac{L_\nu}{h\nu} = \frac{Q(H)}{4\pi R^2 c\, n_H} \tag{1.3}$$

where R is the distance of the cloud, c is the speed of light and $Q(H)$ is the ionizing photon flux. Once U is set as a free parameter it is not necessary to fix the source luminosity and the cloud distance, but only the ionizing SED shape. Although these models are successful in fitting strong optical lines they fail to reproduce certain properties of the NLR and ENLR (Binette et al., 1996).

In comparison with observations these models predict too weak high ionization lines such as [Ne V]λ3426, C IV$\lambda\lambda$1549 and [Fe VII]λ6087, moreover in the ENLR the excitation tends to be even higher than in the NLR. The predicted electronic temperature is, again, too low. This is generally inferred from line ratio $R_{\mathrm{OIII}} =$ [O III] λ4363/[O III] λ5007. Typical observed ratios are $R_{\mathrm{OIII}} \geq 0.015$ in the NLR while models predict significantly smaller values. Another problem is the under-predicted value of He II/H$_\beta$ ratio, that should be independent of the density and the ionization parameter.

1.4.2 Two-zone models

As we have seen single cloud models are unable to account for both high and low ionization lines. At least two gas components are then responsible for the emission. In the literature we found two types of approach: a mix of matter-bounded and ionization-bounded clouds, and a combination of two distinct single-zone models.

The first approach was proposed by Binette et al. (1996) and involves the presence of two distinct class of clouds: matter-bounded are fully ionized regions of gas whose edges are defined by the presence of matter, conversely ionization-bounded clouds are able to absorb all ionizing photons and then they are bounded only by the gas ionization. A schematic representation of this model can be seen in
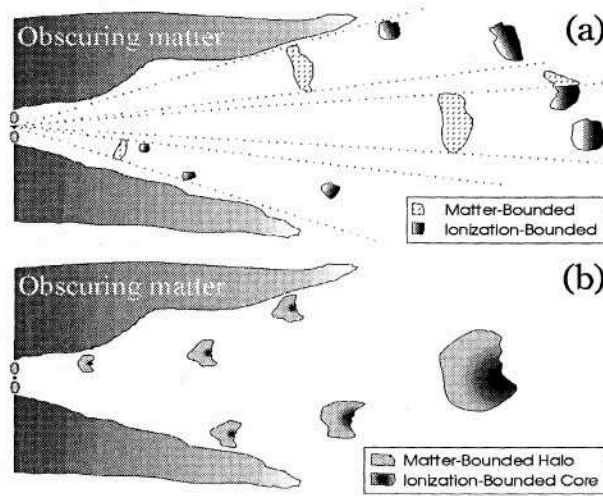
Figure 1.7: Visual representation of the two-zone model proposed by Binette et al. (1996). The dichotomy between ionization-bounded and matter-bounded clouds can arise either from two distinct populations or inside the clouds themselves.

figure 1.7.

The second approach was proposed by Komossa & Schulz (1997) and itis based on the combination of two different cloud models, one responsible of high ionization lines and the other of the low ionization ones.

1.4.3   A note on shocks

Although it is believed that the main ionization mechanism at work in the NLR and ENLR is the photo-ionization from the central source, other mechanisms may play a significant role. This is, for instance, the case of shocks. The NLR exhibits velocities of the order of $v \sim 500\,\mathrm{km\,s^{-1}}$, therefore if clouds are moving in a lower density medium shocks cannot be neglected. The contribution of shocks has been useful in several cases, e.g. in modeling the ENLR of NGC 7212 (Contini et al., 2012; Congiu et al., 2017a) and IC 5063 (Congiu et al., 2017a), and in reproducing the SED of NLS1 galaxies Ark 564 (Contini et al., 2003) and Mrk 766 (Rodríguez-Ardila et al., 2005). To the best of our knowledge, however, shock + photo-ionization codes, such as SUMA (Viegas & Contini, 1994), are limited to a single-zone treatment. Multi-cloud models are feasible by averaging

weighted single-zone models (Contini et al., 2003; Rodríguez-Ardila et al., 2005). A possible, and for the moment unexplored, solution may reside in hybrid photo-ionization / magneto-hydrodynamic codes such as TPCI, an interface between the MHD code PLUTO and *Cloudy*, the famous photo-ionization code (Salz et al., 2015). A solution however relying heavily on computational power.

1.5 The role of Integral-Field Surveys

The spectrophotometric information of a celestial object is generally defined by three dimensions, two of which are spatial (the celestial coordinates) and one is the wavelength (or the frequency). From an historical point of view only two of these dimensions could be used in a single instrument: in the case of photometry the wavelength dimension is integrated over certain limits defined by the adequate filters, while spectroscopy is forced to lose spatial information in the orthogonal direction with respect to the slit. This condition is perfectly acceptable when spectra of unresolved sources are required or when working with integrated magnitudes and the spectral information is not necessary. Neither of these cases are optimal for the study of extended regions of ionized gas such as the ENLR.

Luckily since late 90' a new era of instruments began with the birth of Integral Field Spectroscopy (IFS).

1.5.1 What is Integral Field Spectroscopy?

Integral field spectrographs are instruments that allow the user to collect the spectrum of an object over the whole field of view of the instrument. The main goal of these instrument is to overcome the necessity for multiple slit scanning of the target that were extremely time inefficient and prone to inhomogeneities in the data due to the different observational times.

The integral field spectrograph consists of two elements: the spectrograph and the integral field unit (IFU). The role of the IFU is to subdivide the spatial plane into elements in order to create a continuos array, the pseudo-slit (made exception for the lenslet array, see below). There are three main IFU configurations (see

figure 1.8):

- **Lenslet array**: the input image is subdivided into a bi-dimensional array by microlenses. The light from each element is then focused and goes to the spectrograph. The microlenses array can be tilted about the optical axis in order to avoid superposition of the spectra. The sampling is continuous, however the spectral range is limited to avoid overlapping spectra (Bacon et al., 1995).

- **Fibers**: a 2D bundle of optical fibers is placed where the image is formed and light is transported into a pseudo-slit that goes to the spectrograph. In its simplest design this technique cannot achieve a contiguous sampling since there are gaps between the fibers. This disadvantage can be overcome coupling the fibers with a lenslet array. It is the most common IFU configuration (Barden & Wade, 1988).

- **Slicer**: the image is formed on a mirror composed by thin segments that "slice" the image. Each segment sends the light in a different direction. A second segmented mirror rearranges the slices in a pseudo-slit towards the spectrograph. The main disadvantage is that the optical system may be bulky (Content, 1997).

The majority of modern integral field spectrographs are optimized in the red part of the optical spectrum and in near infrared. This is mainly due to the technical design of the most common configurations. In the case of optical fibers (with or without lenslets) it is difficult to manufacture them with an efficient transmission of blue light. Slicers instead, being mirrors, can be easily cooled, making them an excellent choice for the IR. Considering furthermore that the vast majority of integral field instruments are mounted in ground based observatories, a good adaptive optics system is more or less mandatory. Current adaptive optics (AO) technology is optimized at longer wavelengths and this means that the focus of new IF instrumentation is the red - NIR channel.
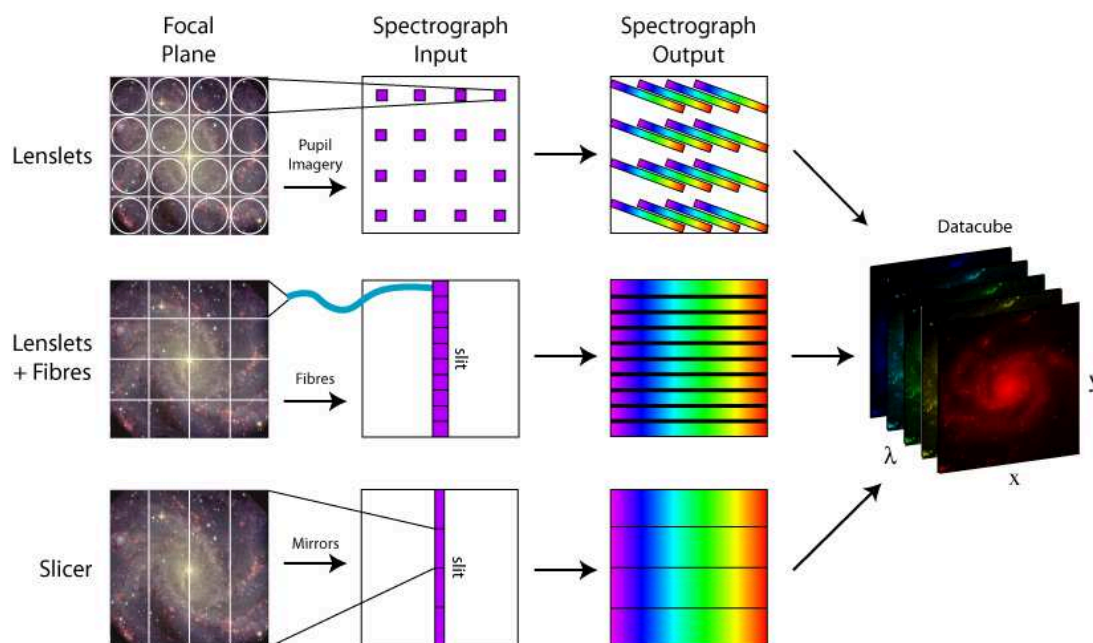
Figure 1.8: A scheme of the three main integral field configurations. Regardless of the chosen configuration the output delivered is a datacube.

1.5.2 Why it is important?

Integral field tries to overcome the traditional disadvantages of long-slit spectroscopy. These include the loss of incident radiation in extended objects, due for instance to poor seeing, and wavelength-dependent effects such as differential atmospheric refraction. Integral field allows to record the spectrum from each part of the extended object, this cannot be done with a long-slit, except by scanning.

The variety of possible scientific targets that can benefit from this kind of instruments is huge and includes all extended sources, from pre-main sequence objects to galaxies, resolved star clusters and, of course, nearby AGN. This is especially true in our case, the study of the extended narrow line region. For instance, the ability to produce line-ratio maps of the ENLR allows to discriminate between ionizing mechanisms in different regions of the galaxy. Furthermore the spectral information allows to build bi-dimensional kinematic maps of the gas, an unprecedented opportunity to shed light on the ENLR phenomenon. Finally with the advent of integral field surveys (see section 1.5.4) it is reasonable to ex-

pect the discovery of new ionization cones in known Seyfert galaxies: the AGN classification relied for many years on slit-spectroscopy and it would not be surprising if a thorough integral field survey revealed many more ENLR in the local universe.

1.5.3   A notable example - MUSE

In the last twenty years integral field technology made giant leaps forward. Right now the state of the art is indisputably represented by MUSE - Multi Unit Spectroscopic Explorer mounted at ESO VLT. MUSE is a massive instrument combining 24 spectrographs with as much slicer IFUs, in order to deliver an outstanding $1 \times 1 \, arcmin^2$ field of view in its wide field mode and a spatial sampling of $0.2 \times 0.2 \, arcsec^2$. To make a quick comparison, the Multi Pupil Fiber Spectrograph (MPFS) made at SAO RAS twenty years ago, had a 16×16 lenslet array plus optical fiber configuration and covered a $16 \times 16 \, arcsec^2$ field of view with a spatial sampling of $1 \, arcsec$.

When the dedicated adaptive optics will be integrated with MUSE and the narrow-field mode will be operational, the field of view will be $7.5 \times 7.5 \, arcsec^2$ and the spatial sampling will reach $0.025 \times 0.025 \, arcsec^2$. This means that for an object with redshift $z = 0.02$ the projected distance resolved by MPFS and MUSE in wide and narrow field mode would be respectively $408 \, pc$, $81.6 \, pc$ and $10.2 \, pc$. It is clear that the study of the NLR or the ENLR could hugely benefit from this new generation of integral field spectrographs.

1.5.4   Surveys

The evident advantages of IFS stimulated in the last few years the first integral field surveys. At the moment there are three major ongoing or completed surveys (details in table 1.2) :

- CALIFA: Calar Alto Legacy Integral Field Area Survey observed a statistically well-defined sample of ~ 600 galaxies. The targets for this survey have been selected from the photometric catalog of the Sloan Digital Sky Survey as a sample limited in apparent isophotal diameter. DR3 was released in 2016 and comprises the datacubes of 667 galaxies.
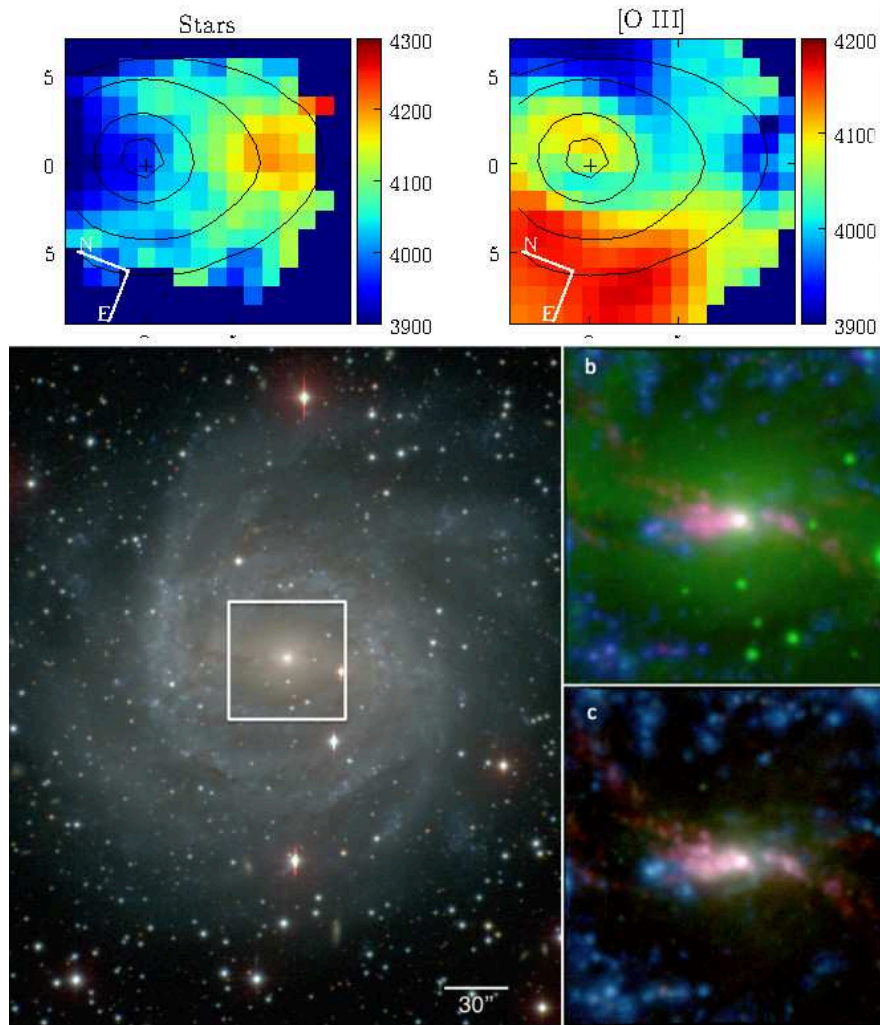
Figure 1.9: Top panel: kinematic maps of Mrk3 realized with MPFS (16×16) lenslet + fiber array (Di Mille 2007, PhD thesis). Bottom panel: NGC 5643 observed with MUSE

- SAMI: Sydney-Australian Astronomical Observatory Multi-object Integral-Field Spectrograph, with a planned observation of ~ 3000 galaxies. The most recent data release is DR1 (2017) with 772 galaxies.

- MANGA: Mapping Nearby Galaxies at Apache Point Observatory. It has a planned observation of ~ 10000 galaxies. One of the key scientific goals is the study of the role of AGN in star formation quenching, we can then reasonably expect that a considerable fraction of the targets will be AGN.

Even if these surveys are not specifically devoted to AGN, a statistical fraction of the targets are indeed active galaxies. In the next few years the probability of serendipitous discovery of ENLR will offer an unprecedented chance to study the key open problems of ENLR such as the origin of gas and the effects of collimation on the ionization cones themselves. In this new era of 3D spectral cubes will rise the need for new ENLR models accounting for spatial effects.

	MANGA	SAMI	CALIFA
Sample size	10000	3400	600
Selection	$M_* > 10^9\,\mathrm{M_\odot}$	$\mathrm{M}_* > 10^{8.2}\,\mathrm{M_\odot}$	$45'' < D_{25} < 80''$
Redshift	$0.01 - 0.15$	$0.004 - 0.095$	$0.005 - 0.03$
λ range (nm)	$360 - 1030$	$370 - 735$	$375 - 750$
σ instrument (km/s)	50 - 80	75 / 28	85 / 150
angular sampling	$2''$	$1''.6$	$2''.7$

Table 1.2: Principal sample selection and instrumental characteristics of the three integral field surveys.

1.6   Aim of this work

In the previous sections we have seen how the ENLR phenomenon is far from being completely understood. The recent developments in integral field spectroscopy and the start of the first integral field surveys are going hopefully to provide an increasing number of AGN with such extended emission. This idea comes from basic considerations: until the first observation of an ENLR (Unger et al., 1987) nobody expected their existence. Over the years, dedicated

imaging surveys and serendipitous discoveries have revealed ~ 50 objects with ENLR in the local universe and similar features in more distant quasars. The increasing number of integral field observations in AGN is likely to make the ENLR a more common feature among AGN.

The aim of this work is to explore a new method to realize bi-dimensional or three-dimensional photo-ionization models of extended regions of gas, focusing in particular on the extended narrow line region. The underlying idea is to treat the ionized gas as a inhomogeneous three-dimensional distribution of local overdensities (clouds or clumps of gas and dust) instead of relying on single-zone or two-zone models. If the various spectral features in ENLR come from clouds of different densities we will try to obtain the same results from a less "artificial" setup.

We developed a code able to procedurally generate a distribution of clouds in a lower density medium with the intent of reproducing a plausible distribution of gas in the ENLR. Furthermore, taking advantage of the same principle, we created a clumpy torus model able to shield the radiation of the central engine and naturally produce di ionization cones in the gas disk. The model creator is integrated with the photo-ionization code *Cloudy* and it is able to generate a user-defined distribution of gas.
The main scientific goals of this work are:

- To create a new approach to model the photo-ionization of a region of gas, taking into account a discrete distribution of clouds.

- To study the effects caused by different torus models on the ionization in the ENLR. Specifically we aim to study angular variations in the ionization near the edge of the ionization cones (as observed for instance in NGC 4151)

- Asses the role of radiation leaking through the gaps between the torus clumps in the ionization of gas in the cross-cone regions.

- Create bi-dimensional models of the ENLR in active galaxies able to reproduce integral field emission line maps.

The Procedural Cloud Generator (PCG) code is focused on a particular scientific case, the ENLR, however the basic tools provided by this software (see sections 2.3.2, 2.3.4 and 2.3.5) can be applied on different subjects, although some kind of adaptation would still be necessary. Moreover the choice of *Cloudy* as photo-ionization code was based on utility: as a matter of fact a set of PYTHON library was already available. We do not exclude that PCG could be integrated with other photo-ionization codes, with the only caveat that these codes should be able to accept a radial density profile as input.

Chapter 2

Code

In this chapter we describe the general outline of the code we wrote to produce the photo-ionization models. In section 2.1 we introduce *Cloudy* (Ferland et al., 2013), the photo-ionization and spectral synthesis code. Section 2.2 is dedicated to the description of PyCloudy (Morisset, 2013), a set of PYTHON libraries devoted to handle the inputs and outputs of Cloudy with the PYTHON LANGUAGE. In section 2.3 we examine the Procedural Cloud Generator (PCG hereafter) that was used to model the gas and dust distribution. Finally in the next chapter (3) we provide an example of the code we used to create the models. In figure 2.1 we represented the code structure in its interaction with *Cloudy*. All the steps will be described in this chapter, not necessarily following the flow direction.

2.1 *Cloudy*

Cloudy is an open source microphysics and plasma simulation code developed by Gary Ferland and collaborators over the last thirty years. The 2013 release, the one utilized in this work, is fully described in its innovations in Ferland et al. (2013). The goal of *Cloudy* is to simulate conditions in a non-equilibrium gas and predict its spectrum, the element ionization, the level populations and thermal state. The range of temperatures extends form the CMB temperature up to 1.001×10^{10} K, and the applications vary from H II regions to the ionized gas around a supermassive black hole. It was first designed to simulate the dense gas in the Broad line Region in AGN, but since then constant improvements allowed
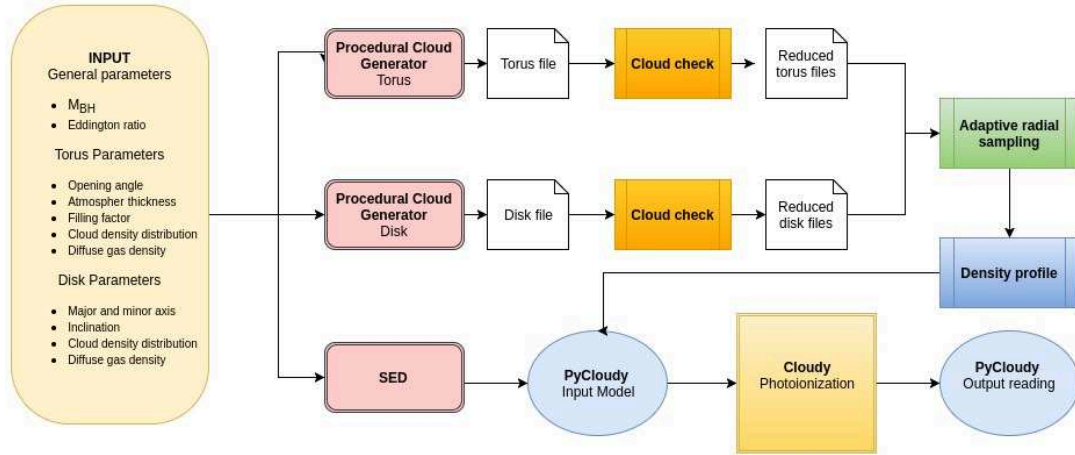
Figure 2.1: Code structure flowchart. The user defines a set of free parameters from which the gas distribution is generated (in this case torus+disk) and the SED is re-scaled in luminosity. The gas distribution is then sampled in radial directions originating from the ionization source and a radial density profile is computed. The input parameters are passed to Cloudy that performs the radiative transfer calculations and computes the gas ionization.

much wider applications.

Cloudy allows to specify a wide set of parameters to build the models, often when a parameter is not set the default option is assumed. However some components must be specified.

The incident radiation field

Both the shape and intensity of the external field hitting the cloud must be specified. The shape of the spectral energy distribution (SED) should be defined between an energy of 1.001×10^{-8} Ryd ($\lambda \approx 10$ m) and an energy of 7.354×10^{6} Ryd ($h\nu \approx 100$MeV), where 1 Rydberg is approximately the ionization potential of hydrogen. This can be specified through built-in functions such as blackbody emission, power-law with exponential cut-offs or AGN spectral energy distribution, it can be interpolated from table, or the radiation field transmitted through a cloud predicted by previous calculations.

The SED is then re-scaled on the basis of the intensity of the radiation field. This can be given either as a flux or as luminosity radiated by the central object into 4π sr. The code must be able to derive the flux of photons striking the illuminated face of the cloud. Up to 100 different radiation fields can be combined together in the same calculation.

Density and chemical composition

The cloud density is given in terms of neutral hydrogen (HI) density, while the other elements abundances can be specified (otherwise solar abundances are assumed). The code treats in detail the lightest 30 elements. The code chemistry also includes many molecules (e.g. H_2 and CO) and will treat them if conditions are met. Dust grains are not part of the default composition but can be included (see appendix A). The grain model in *Cloudy* includes all relevant processes: absorption and scattering of light including stochastic heating effects, the photoelectric effect, collisional charging (electrons as well as atomic ions), thermionic emissions, collisional energy exchange between the grains and the gas, and a calculation of the grain drift velocity.

A remarkable possibility is to give as input a table of coupled radii and density, that is a density profile, which prompted us the idea at the base of PCG. This will be explained in detail in section 2.3.

2.2   PyCloudy

Cloudy is a powerful tool, however is intended to perform only one-dimensional calculations. PyCloudy (Morisset, 2013) is a set of PYTHON libraries designed to overcome this limitation. It is conceived to simplify the setup of grids of models in a user-friendly language, showing its full potential in notebooks (e.g. ipython, jupyter). In section 3 we present an example of model creation using both PyCloudy and PCG to clarify the use of these libraries.

A partial list of PyCloudy features is:

- The possibility to define and write multiple *Cloudy* input files. It can be be integrated in another code allowing to change parameters from one file

to the other automatically. Without these libraries the user could anyway rely on the built-in grid command in *Cloudy*, having anyway to write down manually the input files.

- Read the output files, manipulate and plot the desired quantities. This allows a simple interaction with other PYTHON libraries such as matplotlib, numpy, scipy and astropy.

- Create pseudo 3D or 2D models interpolating a set of models following angular laws in a 3D cube, realizing maps of the desired quantities (T_e, n_e, line emissivities, etc.)

2.3   Procedural Cloud Generator

The emission line spectra of extended regions we observe in Type 2 AGN is difficult to reconcile with simple single-zone models. The introduction of two-zone model led to a better understanding of the ionization in the ENLR. However, applying this ad hoc model to a spatial description of the ionization in the ENLR is a complex task. A possible path in improving our current understanding of photo-ionization models is to provide a reasonable description of the gas and dust distribution in the galaxy and in the torus surrounding the source of the ionizing radiation.

The one-dimensional approach of *Cloudy* seems to be unfit to reproduce bi-dimensional models, however several one-dimensional runs can be interpolated to create pseudo 2D or 3D models by means of interpolation.

We developed a simple python code that allows us to generate a distribution of gas following a set of user-defined assumptions. The output of the code consists in a number of text files containing information about the clouds position, dimension and mass. The integration with the PyCloudy libraries is intended to quickly produce the input files of the photo-ionization code *Cloudy*, given a chosen set of parameters. In this section we outline the code structure and the physical assumptions behind it.

2.3.1 Assumptions

As for the vast majority of simulations and generally speaking the realization of models, we rely on a number of assumptions and simplifications. This is an unavoidable step when the goal is to best describe complex systems of which we have limited information.

The first important assumption regards how the gas is distributed. We decided to give a certain freedom to the user when choosing how to model the gas distribution. The gas can be considered as a two component mixture: one smooth and less dense, the diffuse component, and another denser and localized, the cloud component. Clouds act as over densities with respect to the diffuse component. Each cloud is considered spherical and has a fixed radius (see below for a detailed description). The user can choose to neglect entirely the presence of clouds (or clumps) and consider only the diffuse component, on the other hand it is not possible to cancel the latter because *Cloudy* requires gas densities greater than zero. Of course it is possible to lower significantly the contribution of the diffuse gas.

The second assumption is the role of shocks throughout the ENLR. Several authors pointed out that shocks may play a crucial role in the ionization of gas. For instance the study of diagnostic diagrams of different velocity components in the ENLR seems to indicate that shocks may contribute to lower the degree of ionization in the regions corresponding to high velocities (Contini et al., 2012; Congiu et al., 2017c). This seems to be the case of objects in which the role of jets and outflows is prominent, or when the origin of ionized gas can be attributed to merger events. It should be noted that the principal mechanism remains the photo-ionization by the active nucleus. In our work we decided to focus on the latter and the role of the torus in the collimation process. The main obstacle in the introduction of shocks in the calculation is that their contribution is local and obviously depending on the gas kinematics. Other devoted codes, such as SUMA (see Viegas-Aldrovandi & Contini 1989; Contini & Aldrovandi 1983 and reference therein), already consider the contribution of

shocks, however limited to a "single cloud" treatment.

Finally a word should be spent on how the bi-dimensional models are realized. The ionization map of the ENLR is obtained through the interpolation of several one-dimensional calculations performed by *Cloudy*. This means that each direction along which *Cloudy* runs does not "talk" to the others, i.e. the emission from a single region located at a certain distance from the central ionization source does not influence other neighbour regions. This kind of approach also does not allow to introduce other sources of ionization such as shocks (as seen above) or H II regions embedded in the gas itself.

The only source of ionization is therefore the active nucleus itself; this kind of approach is not well suited to study the contribution of different ionization mechanisms.

2.3.2   The cloud

The cloud is as a python object defined by the coordinates of its center, its radius and its mass. Complex geometries and shapes have not been considered for the single cloud but may arise during the generation by superposition of different clouds. Each cloud is spherical and has a Gaussian mass profile, its radius can be set in relation to the σ of the mass distribution. The definition of its boundary is therefore artificial and introduces an error when the filling factor is set (see cloud generation). However setting the radius to 3 σ is sufficient to consider the error negligible.

Class properties

We list and describe the properties and methods of the cloud object class as defined in the code. The *init* section is the constructor, i.e. the set of parameter given as input when creating the cloud object.

```
__init__:
```

- x_0, y_0, z_0: center coordinates

- r_{cl}: cloud radius

- M_{cl}: cloud mass

Derived properties:

- $\sigma = r_{cl}/3$: σ of the density profile

- ρ_0: central density

- V_{cl}: cloud volume

- ρ_m: mean density

Class methods

- `density`: it calculates the density at given Cartesian coordinates

- `dens_profile`: it accepts as input an array r and the angles θ and ϕ. It calculates the density profile along the array after transforming from spherical to cartesian coordinates calling `density` and returns the density array calculated in each point of r.

The density profile of the cloud is defined as:

$$\rho = \rho_0 \exp \frac{-(x^2 + y^2 + z^2)}{2\sigma^2} \tag{2.1}$$

where ρ_0 is the central density

$$\rho_0 = \frac{m_{tot}}{(2\pi\sigma^2)^{\frac{3}{2}}} \tag{2.2}$$

The choice of a Gaussian density profile over a simpler one (e.g. uniform) is done to avoid steep increases of the gas density when calculating the overall density profile and to provide a more realistic description with little effort. These clouds represent over-densities in the distribution of gas and are surrounded by diffuse, less dense gas. The density of this diffuse component is set separately when the disk, torus or cone object is created.

The cloud mass distribution

For each possible geometric distribution of the clouds it is necessary to determine
the mass distribution. The distribution represents the probability the probability
to create a cloud with a certain mass.

We know from spectroscopy and photo-ionization models (e.g. Binette et al.
(1996)) that the gas in the Narrow line Region cannot be distributed smoothly
and have to present denser aggregations. However how these clouds are actually
distributed in terms of mass and dimension is still an open topic.

The choice of the distribution is left to the user as a free parameter. The default
option is a log-normal distribution. A variable x follows a log-normal distribution
if its natural logarithm is normally distributed. This means that the probability
distribution function is

$$p(x) = \frac{1}{\sigma x \sqrt{2\pi}} e^{-\frac{(\ln(x) - \mu)^2}{2\sigma^2}} \tag{2.3}$$

where μ and σ are the logarithmic analogues of mean and standard deviation of
a classical normal distribution.

The choice of the log-normal distribution is a convenient one, often utilized
to describe the properties of random fields, such as for the distribution of matter
in the Universe (e.g. Coles & Jones 1991 and references therein) or the ISM on
a Galactic scale (Leroy et al., 2016; Berkhuijsen & Fletcher, 2015). Therefore we
consider the log-normal distribution of the cloud masses a safe assumption.

2.3.3   The ionizing SED

Before focusing on the gas distribution we discuss now the source of ionization.
As specified in 2.3.1, the only source of ionizing radiation considered in our
models is the AGN itself. *Cloudy* offers a wide choice of incident radiation fields,
however we only need an AGN-like spectral energy distribution. The built-in
function provided by *Cloudy* produces a multi-component continuum similar to
that of typical AGN, as can be seen in figure 2.2.

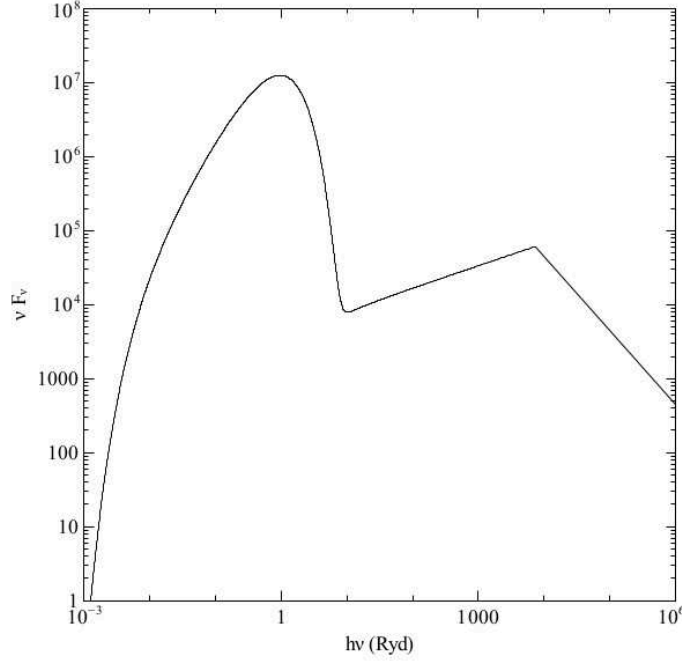The continuum is a sum of two components as can be seen in equation (2.4)

Figure 2.2: Spectral energy distribution produced by the AGN continuum command as described in the *Cloudy* documentation (Hazy 1).

$$f_\nu = \nu^{\alpha_{uv}} e^{\left(\frac{-h\nu}{kT_{BB}}\right)} e^{\left(\frac{-kT_{IR}}{h\nu}\right)} + a\nu^{\alpha_{ox}} \tag{2.4}$$

The "Big Bump" component peaks at 1 Ryd (13.6 eV). It is a rising power-law with an exponential cut-off at high-energy, parametrized by the temperature T_{BB}. The second parameter is α_{ox}, the X-ray to UV ratio. The value is typically $\alpha_{ox} \sim -1.4$ in AGN (Zamorani et al., 1981). The low energy slope of the Big Bump coninuum is set to a default value $\alpha_{uv} = -0.5$ (Elvis et al., 1994; Francis, 1993). In the last term of equation (2.4), $\alpha_x = -1$ is the default value of the X-ray slope and a is a parameter which is automatically adjusted to produce the correct α_{ox}. The exponential low-energy cut-off causes the incident continuum to have zero intensity at long wavelengths. *Cloudy* requires the incident continuum to be defined and different from zero at each energy otherwise it returns an error. This can be prevented adding a CMB background component, which does not influence the calculations.

The SED defined above is then re-scaled by the code taking into account the AGN luminosity L_{agn}, which is determined during model creation. There are only two free parameters involved in the luminosity determination: the black hole mass M_{BH} and the Eddington ratio η. The Eddington ratio is defined as $\eta = L_{agn}/L_{Edd}$, where L_{Edd} is the Eddington luminosity. It is a "limit" luminosity, obtained by setting the outward radiation pressure equal to the inward gravitational force.

$$L_{\mathrm{Edd}} = \frac{4\pi G M_{\mathrm{BH}} m_{\mathrm{p}} c}{\sigma_{\mathrm{T}}} = 1.26 \times 10^{38} \left(\frac{M_{\mathrm{BH}}}{M_{\odot}} \right) \mathrm{erg/s} \qquad (2.5)$$

where m_{p} is the proton mass, σ_{T} is the Compton scattering cross-section for the electron and c the speed of light. The Eddington luminosity depends only on the black hole mass, in this way we can estimate the AGN luminosity setting two free parameters.

The AGN command is not the only useful choice for the user. If the nuclear SED of the source is known, it is possible to use it instead of the default AGN SED. The INTERPOLATE command allows to enter up to 13000 ordered pairs of $\log(\nu(\mathrm{Hz}))$ and $\log(f_{nu})$, and it performs a linear interpolation in log-log space. The interpolated SED will be then utilized in the calculation.

2.3.4   Torus

The definition itself of torus is still an open problem in astrophysics. We refer to the central obscurer as "torus" even if we are not implying a similarity between the shape of the obscurer and the geometric torus.

Our goal is to provide a reasonable model of the central obscurer in order to study the impact on the ionization of gas located far away from the torus itself. The study of the clumpy torus SED is beyond the scope of this work and has been thoroughly described by several authors (e.g. Nenkova et al. 2008a, Nenkova et al. (2008b) , Siebenmorgen et al. (2015)). We follow some assumptions of these works to create our torus model.

The principal feature of the model is the clumpiness: the gas and dust are

distributed in an axisymmetrical configuration only from a general point of view. Locally, matter is concentrated in denser clouds, or clumps, scattered in the region with a predetermined distribution. Therefore the torus is procedurally generated, i.e. the position of the single cloud is randomly determined following a set of rules decided by the user. The most simple choice is of course a uniform distribution in space, meaning that a cloud has an equal probability of being generated in each point inside the torus region. Other spatial distributions will be discussed later.

Class properties

`__init__`:

- R_{in}: inner radius of the torus

- R_{out}: outer radius

- ξ_{oa}: opening angle

- ϕ_T: volume filling factor

- ρ_{diff}: density of the diffuse gas component

- r_{cl}: cloud radius

- m_{cl}: array of possible masses (see 2.3.2 for details)

- p_m: probabilities associated with each mass

- β: angle associated with the putative atmosphere (see 2.3.4)

Derived properties:

- $\alpha = \pi/2 - \xi_{oa}/2$

- $s = \tan(\alpha)$: it is the slope of the torus edge, needed as a boundary during cloud generation

- $V_T = \frac{2}{3}\pi\, s\, (R_{out}^3 - R_{in}^3)$: the volume of the torus

- $V_{cl} = \frac{4}{3}\pi r_{cl}^3$: cloud volume

- $n_{cl} = \phi_T \frac{V_T}{V_{cl}}$: number of generated clouds (rounded to the nearest integer)

Class methods

- `print_properties`: it prints a summary of the parameters used to create the torus

- `gen_clouds`: it generates the clouds and prints their properties on an output file

- `get_diffuse_profile`: it calculates the diffuse gas density profile along a given direction

The shape of the torus

The torus region is defined by three parameters: R_{in}, R_{out} and the opening angle α (see fig. 2.3). The opening angle is related to the height-radius ratio of the torus, however we consider it a free parameter.

There is not yet consensus on the mechanism providing vertical stability to the torus. Possible mechanisms are turbulent or outflow motion (Beckert & Duschl, 2004), optical, UV and IR radiation pressure (e.g. Hönig & Beckert 2007), magnetic winds (Emmering et al., 1992) or star formation in the infalling gas. All of the above mechanisms were included in the three-dimensional hydrodynamic simulation of Wada et al. (2009a) and Wada et al. (2009b).

R_{in} and R_{out} are strictly linked to the AGN luminosity. The inner boundary of the torus is determined by the dust sublimation radius. For our model we adopt a simple estimate of the torus inner boundary, obtained through dust reverberation mapping (Koshida et al., 2014). This is, of course, a simplified model, not intended for the calculation of the torus SED or to simulate the emission lines of the inner boundary, but only to provide a reasonable obscuring object with features able to influence the collimation of the ionizing radiation.

The maximum radial extension R_{out} is dependent on the sublimation radius $R_{sub} \sim R_{in}$ as:
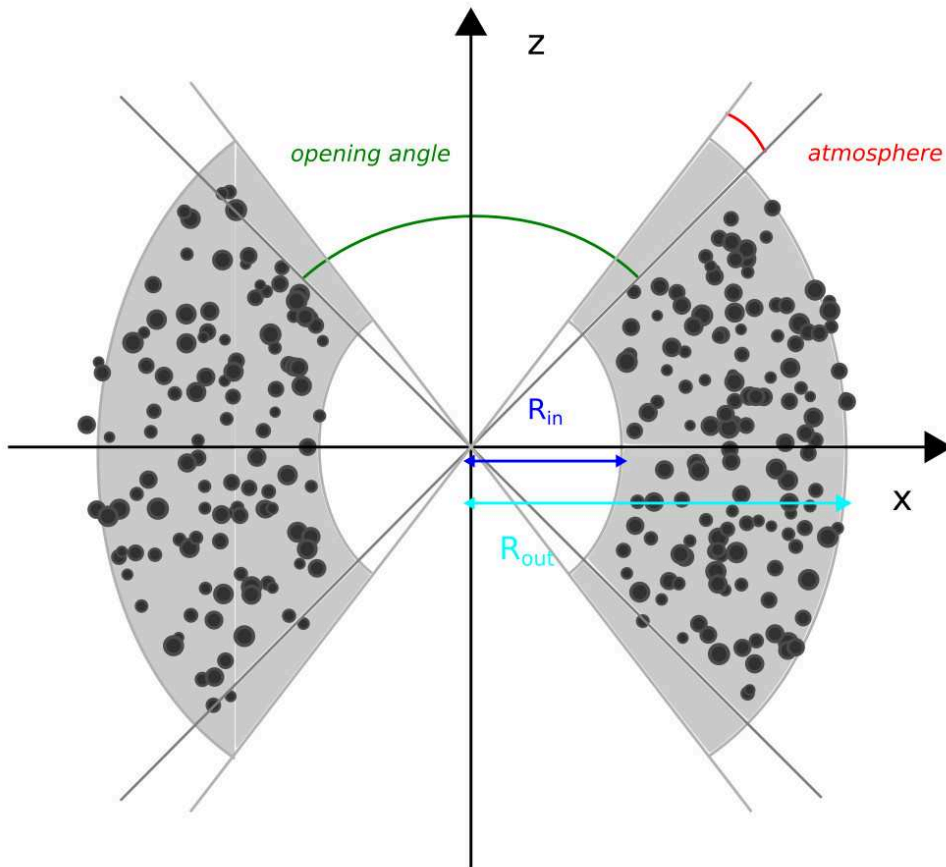
$$R_{out} = k\, R_{in}$$

Figure 2.3: Sketch of the torus geometry: the figure represents a 2D cut meant to illustrate the principal geometric parameters involved in the torus generation.

where k is a scale parameter. In the literature we found different values of k ranging from ~ 20 up to $k = 170$ (Siebenmorgen et al., 2015). We adopted the latter value but it is important to stress that it is only a conservative choice and we have no evidence on the actual extension of the torus but only on the inner boundary.

Cloud generation - spatial distribution

The cloud generation inside the torus is performed by the `gen_clouds` method. It is based on a series of bounded random number generations for all the cloud parameters. It depends on the chosen spatial distribution but only in a minor

fashion. The main parameter in the generation is the total number of clouds n_{cl}, that is function of the filling factor and of the cloud and torus volumes. The method will continue to generate clouds until this number is reached.

The user can choose between two spatial distributions: uniform and z-gaus. The latter is uniform on the x-y plane but follows a normal distribution on the z coordinate.

For each cloud the process is as follows:

1. x_0 coordinate is picked from a uniform distribution bounded by $-R_{out}$, $+R_{out}$;

2. y_0 coordinate is generated in the same way but the boundaries are modified by x_0: $(-\sqrt{R_{out}^2 - x_0^2}$, $+\sqrt{R_{out}^2 - x_0^2})$;

3. radial distance from the center is checked to avoid clouds inside R_{in};

4. z_0 coordinate is picked from a uniform or normal distribution, depending on the user's choice. The boundaries for the uniform case depend on the x_0 and y_0 coordinates, in the form $(-r \tan\alpha, +r \tan\alpha)$, where $r = \sqrt{x_0^2 + y_0^2}$. In the z-gaus case the same $r \tan\alpha = 2\sigma$;

5. the total mass of the cloud is then picked from a distribution chosen by the user;

6. all the parameters are printed on the output file;

7. repeat from 1 until n_{cl} is reached.

In figure 2.4 it is possible to see the difference between the two spatial distribution for a torus generated with the same parameters.

The atmosphere

When considering the distribution of gas and dust in the torus one should not exclude the possibility that the transition between the torus itself and the NLR
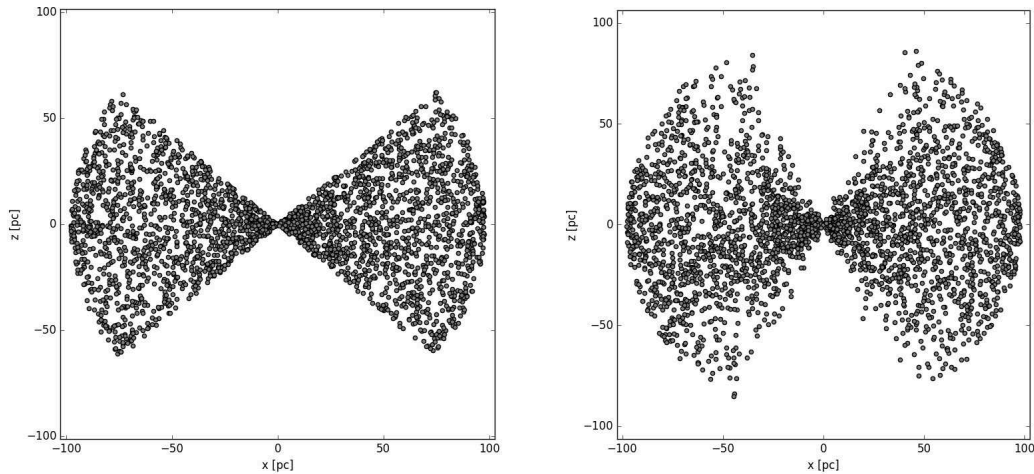
Figure 2.4: Side-cut of the generated clumpy torus. Each point is the position of one cloud center. The width of the cut is R_{in}. On the left panel: uniform cloud distribution. On the right: z-gaus distribution.

might be smooth instead of being sharp. The presence of this putative atmosphere has been suggested by Tsvetanov et al. (1996) as a possible interpretation of the peculiar features observed in the Seyfert 1.5 galaxy NGC 4151. The spectrum of this object shows clearly a broad line component in the emission lines, implying that the line of sight of the observer towards the innermost region of the AGN is relatively clear. However [OIII] images of the galaxy reveal extended ionization cones. The proposed solution was that a region of lower column densities with respect to the torus was responsible of the absorption of the ionizing radiation coming from the nucleus. The intervening warm absorber is able to block the X-ray and UV ionizing radiation but not optical one, therefore letting a clear view to the broad line region. A similar explanation has been proposed for the X-ray absorption in Mrk 6 (Feldmeier et al., 1999).

To take into account this possibility we introduced another free parameter in the for of an angle β. The atmosphere hence is a region located on the edge of the torus where clouds are not generated (in the uniform distribution case) or have lower probability of being generated (z-gaus case) but still provides absorbing material in the form of a diffuse gas and dust component (see figure 2.3).

Diffuse gas density profile

The smooth component of the gas (and dust) in the torus can be chosen between two options: a uniform distribution and a composite Gaussian function. The `get_diffuse_profile` method takes as input a radius array r and the angle θ, identifying an array of points in polar coordinates. It is valuable to consider that even if the torus is defined in three dimensions, its axial symmetry allows us to neglect the angle ϕ. The method then proceeds to calculate the densities in agreement with the chosen profile and it assigns them to another array with length equal to r.

The uniform distribution is straightforward: if the points in r (considered θ and ϕ) are inside the torus the assigned density value will be ρ_{diff}, otherwise it will be fixed to zero.

The other option, the composite Gaussian function, is defined as:

$$\rho = \rho_0 \, e^{-\left(\frac{r-\mu_r}{\sigma_r}\right)^2 - \left(\frac{\theta - \pi/2}{\sigma_\theta}\right)^2} \tag{2.6}$$

where

$$\mu_r = (R_{out} + R_{in})/2$$
$$\sigma_r = (R_{out} - R_{in})/2$$
$$\sigma_\theta = \alpha + \beta$$

as defined in section 2.3.4. An example of this profile can be seen in figure 2.5.

2.3.5   Disk

After having discussed how the obscuration of the torus is modeled, we focus on the gas distribution in the galactic disk. The problem of the origin and actual distribution of the gas is complex and specific for each object, and it has not been addressed in this work. From what we observe in the Milky Way, neutral hydrogen lies almost entirely on the Galactic disk and it is locally concentrated in the spiral arms (Nakanishi & Sofue, 2016). Neutral hydrogen is a good tracer of gas distribution in galaxies, given its sheer abundance, and it is the primary
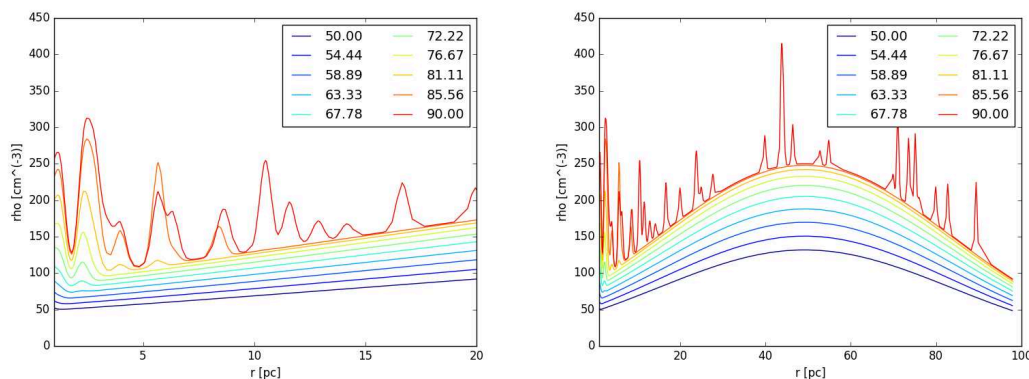
Figure 2.5: Density profiles of the torus at different angles θ. The diffuse gas distribution is the composite Gaussian, while the spikes in the profiles are clouds encountered in that direction. The density values are very low with the purpose of being shown. More realistic densities for torus clumps are in the range $10^4 - 10^5\,cm^{-3}$.

input of *Cloudy* when considering gas densities. All the other elements are considered as abundances with respect to HI (see 2.1).

The use of neutral hydrogen is of course a proxy, given that the gas we observe in the ENLR is ionized and its origin is still debated. However we can safely assume that without an active nucleus a large fraction of this gas would be neutral, being the AGN the main ionization mechanism. That is the reason why the construction of our model is partly based on studies referring to the distribution of neutral gas in galaxies, and partly on information we have from the analysis of the emission of ionized gas, such as the presence of clouds.

From what we observe in the observations of ENLR with interference filters (mainly [OIII]) the actual geometry of the ionized gas is far more complex and would need devoted studies for each object to be modeled. This kind of study is in principle feasible with PCG, however we preferred to focus on a general approach rather than a specific description of a single object. For this reason the gas is distributed in a disk, without any specific consideration about spiral arms or other local concentrations, made exception for the clouds themselves.

The disk is an oblate ellipsoid in which the two major axes are equal and can be oriented with respect to the torus axis to reproduce the general lack of

correlation between the galaxy and AGN orientations.

Class properties

`__init__`:

- a,b: major and minor semi-axis

- R_{in}: an inner empty radius where the torus is placed

- α: the inclination angle

- ϕ_{D}: volume filling factor of the disk

- ρ_{diff}: density of the diffuse gas component

- r_{cl}: cloud radius

- m_{cl}: array of possible masses (see 2.3.2 for details)

- p_m: probabilities associated with each mass

Derived properties:

- $V_d = \frac{4}{3}\pi a^2 b - \frac{4}{3}\pi R_{in}^3$: volume of the disk, subtracted the inner sphere

- $V_{cl} = \frac{4}{3}\pi r_{cl}^3$: cloud volume

- $n_{cl} = \phi_{\mathrm{D}} \frac{V_d}{V_{cl}}$: number of generated clouds (rounded to nearest integer)

Class methods

- `rotate`: during cloud generation it applies a rotation to the center coordinates according to the inclination angle α

- `print_properties`: it prints a summary of the parameters used to create the torus

- `gen_clouds`: it generates the clouds and prints their properties in an output file

- `get_diffuse_profile`: it calculates the diffuse gas density profile along a given direction

The geometrical shape of the disk is simple, the only deviation from the oblate ellipsoid is in the form of a spherical cavity in the center. This void area is intended to house the torus and avoid the generation of clouds inside this region.

Cloud generation - spatial distribution

As for the torus, the cloud generation in the disk is performed by the `gen_clouds` method and it depends on the chosen spatial distribution. The user choices are two: the usual uniform distribution and a normal distribution that concentrates the clouds towards the center (see figure 2.6). The number of generated clouds depends as usual on the volume filling factor ϕ_D and on the disk and cloud volumes. The step-by-step process is similar to the torus one and it is reported below:

1. x_0 coordinate is generated between $(-a, +a)$ for the uniform case, while in the Gaussian case the semi-axis acts as σ;

2. y_0 is generated in the same way but limits and σ are changed to $\sqrt{a^2 - x_0^2}$;

3. z_0 is generated as above but with limits $\pm b\sqrt{1 - \frac{(x_0^2 + y_0^2)}{a^2}}$;

4. if the cloud is outside the inner radius, the coordinates are changed by `rotate`, then the mass is assigned according to the chosen distribution and the cloud parameters are printed in the output file;

5. the process repeats from 1 until n_{cl} is reached.

Diffuse gas density profile

Three different options are available for the disk diffuse gas density profile. Leaving aside the self-explanatory uniform profile, the other two are worth a few words. In all the profiles the diffuse density parameter ρ_diff plays a different role,
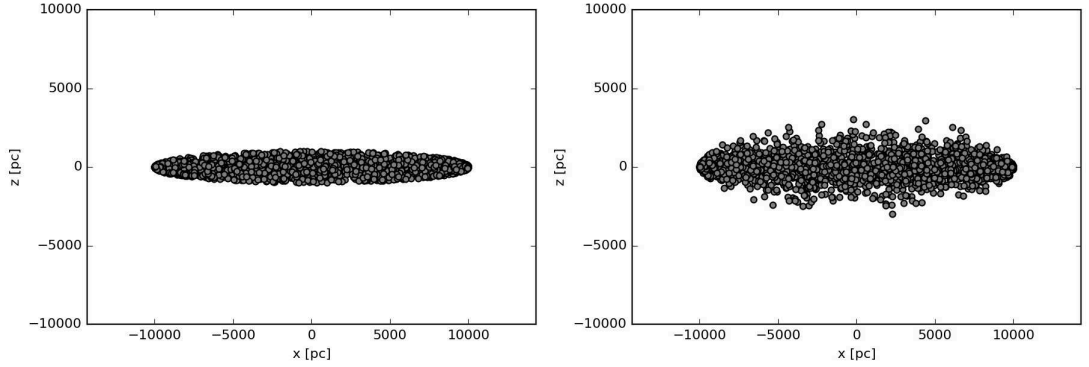
Figure 2.6: Side-cut of the generated disk. As for the torus in figure 2.4, the only difference is the choice of cloud distribution.

in the uniform case for instance it is the density assigned to each point inside the disk. In the others it acts as a reference density that is combined with a scale radius.

The first one is a decreasing exponential profile, similar to the one observed in the outer part of gas-rich galaxies (Wang et al., 2014). It is defined as

$$\rho = \rho_{\text{diff}} \; e^{-\frac{r}{r_s}} \tag{2.7}$$

where r_s is a scale radius defined by the user. The value of ρ_{diff} should be adjusted in accordance with the scale radius to obtained the desired density profile.

The last option is a power-law profile:

$$\rho = \rho_{\text{diff}} \; \left(\frac{r}{r_s} \right)^{-\mu} \tag{2.8}$$

where μ is a free index with default value $\mu = 2$. This profile has not a physical base but it is intended for test purposes.

2.3.6   Cone

The cone object is designed to create one-dimensional models taking advantage of the three-dimensional approach of PCG. Its scope is to reduce the computational time when the whole galactic disk is not needed. It is important to stress that, even if the name may be misleading, it is not intended to model specifically the

ionization cones. As the name suggests, this class object creates a truncated cone region in which the clouds are generated. The spatial distribution of clouds is strictly uniform and the diffuse gas density profiles are the same of the disk class (see section 2.3.5).

Class properties

`__init__`:

- h_{in}: distance from the source where the minor base is placed

- h_{out}: distance from the source of the major base

- β: opening angle of the cone

- ϕ_c: volume filling factor

- ρ_{diff}: density of the diffuse gas component

- r_{cl}: cloud radius

- m_{cl}: array of possible masses (see 2.3.2 for details)

- p_m: probabilities associated with each mass

Derived properties:

- $\alpha = \left(\frac{\pi - \beta}{2}\right)$

- $\tan \alpha$: slope of the cone edge

- $V_c = \frac{1}{3}\frac{\pi}{\tan^2 \alpha}(h_{out} - h_{in})(h_{out}^2 + h_{in}^2 + h_{in}h_{out})$: volume of the cone

- V_{cl}: volume of the cloud

- $n_{cl} = \phi_c \frac{V_c}{V_{cl}}$: number of generated clouds

Class methods

- `print_properties`: it prints a summary of the parameters used to create the cone
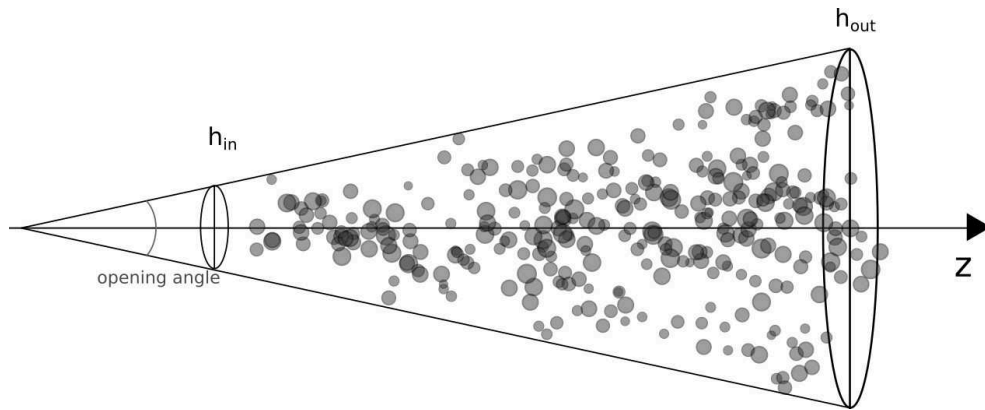
Figure 2.7: Visual representation of the cone object.

- `gen_clouds`: it generates the clouds and prints their properties in an output file

- `get_diffuse_profile`: it calculates the diffuse gas density profile along a given direction

Cloud generation - spatial distribution

Similarly to the classes described above, the cloud generation is a series of random draws repeated until the target number of clouds is reached. However due to the small volume and the simpler rules it is far less computationally intense. Refer to figure 2.7 for the cone geometry.

1. z_0 coordinate is drawn froma uniform distribution bounded by (h_{in}, h_{out});

2. x_0 is similarly generated between $(-\frac{z_0}{\tan\alpha}, +\frac{z_0}{\tan\alpha})$;

3. y_0 as above but with limits $-\sqrt{\left(\frac{z_0}{\tan\alpha}\right)^2 - x_0^2}, +\sqrt{\left(\frac{z_0}{\tan\alpha}\right)^2 - x_0^2}$;

4. the mass is assigned according to the chosen distribution and the parameters are printed in the output file;

5. it repeats from 1 until n_{cl} is reached

2.3.7 Radial sampling of the gas

Once all the model objects have been generated the radial density profile is calculated. It is necessary to define several arrays r_i containing the points where the density will be calculated. Each one of these arrays have to be associated to a direction, identified by the spherical coordinates θ and ϕ (see figure 2.8).

The choice of these angles can be tricky. Ideally the best choice would be to select a very large number of directions (θ, ϕ) to be sure that the space is sufficiently covered. However each one of these direction is a separate model run by *Cloudy*, requiring a certain computational time (from few minutes to several hours), so the "full coverage" option may not be the best choice. A possible solution is to draw the angles from a uniform bounded distribution, performing a random sampling. Another strategy for bi-dimensional models is to fix ϕ and assume axial symmetry, while letting θ vary between 0° and 90°.

The definition of the r_i arrays is however more complicated and it is described in the following sections.
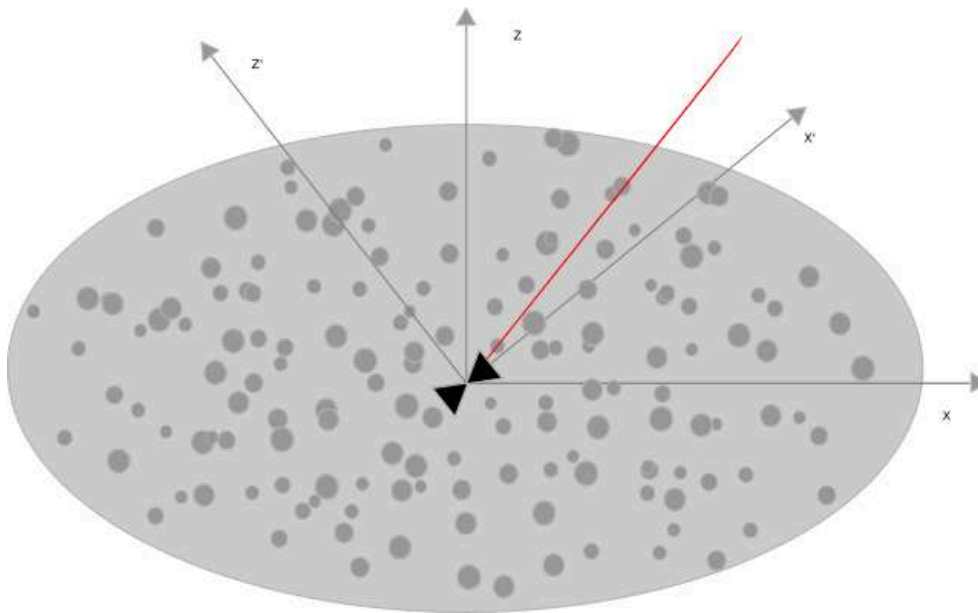

Figure 2.8: Visual representation of how the density profile is calculated. After the chosen objects (i.e. torus and disk) are populated with clouds, the density is calculated along a line (red line in the picture) starting from the center of coordinates, where the ionizing source is placed.

Cloud check

Given the sheer number of clouds generated for a single object (the torus or the disk) it is helpful to reduce smartly the number of clouds involved in the density profile calculation. To accommodate this necessity a separate routine was introduced: check_clouds.

The density profile is a one-dimensional array identified by a single direction in space originating in (0,0,0), where the ionization source is located. This direction is described in spherical coordinates by two angles, θ and ϕ. The idea is to check which clouds are intersected by a straight line along the same direction.

A straight line equation can be written in parametric form as

$$\vec{x} = \vec{p} + t\vec{v} \tag{2.9}$$

where $\vec{p}$ is a point along the straight line, (0,0,0) in our case, and $\vec{v}$ is the direction of the line. The straight line equation can be written as $\vec{x} = t\vec{v}$. The vector $\vec{v}$ is determined from spherical coordinates imposing the radial coordinate $\rho = 1$

$$v_1 = \rho \sin\theta \cos\phi \tag{2.10}$$

$$v_2 = \rho \sin\theta \sin\phi \tag{2.11}$$

$$v_3 = \rho \cos\theta \tag{2.12}$$

substituting $\vec{x}$ in equation 2.13, where $\vec{c}$ is the center and r is the radius

$$(x_1 - c_1)^2 + (x_2 - c_2)^2 + (x_3 - c_3)^2 = r^2 \tag{2.13}$$

one obtains a second degree equation in t. The clouds whose surface is tangent or intersected by the ray direction are saved in a separate file. This process is necessary for the next step in the calculation of the density profile.

Adaptive radius

Cloudy accepts as input a density profile in the form of a table of paired radii and densities. The profile is then calculated by linear interpolation in a Log-Log

plane. A maximum of 500 pairs is accepted, hence it is important to choose wisely these pairs in order to retain the maximum information while sampling the gas distribution. For instance, choosing a uniform or logarithmic spacing, there is a non-zero probability that a cloud would fall entirely between the point of the array.

The adaptive sampler function calculates where the ray direction intersects the clouds, sampling them uniformly with a user-defined number of points. Between each cloud other points are added to take into account the gas diffuse component. The sampling of the cloud is obtained following the same method of the check_cloud function. The parametric solutions t_1 and t_2 represent the point of intersection of the line of sight with the cloud. The Euclidean distance l between the two points is then calculated and the segment is subdivided in k equal parts, where $k = l/(n_{points} - 1)$ (see figure 2.9).
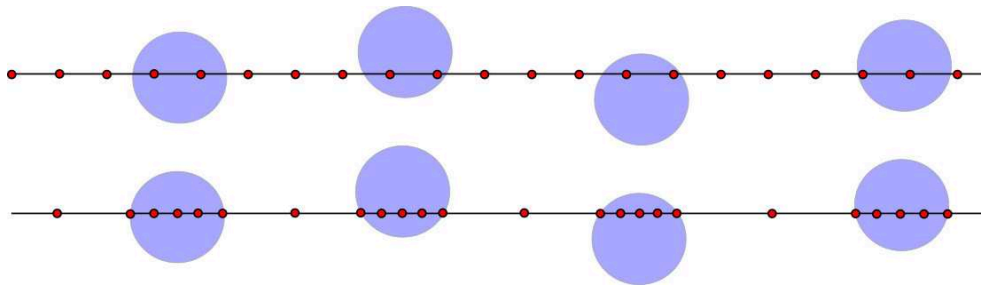
Figure 2.9: Example of adaptive sampling with five sampling points for the clouds and one point in between.

Points removal

Given the hard limit on the number of couples accepted as input by *Cloudy*, one should in principle consider the case in which a large number of clouds is intersected by the line of sight. Moreover *Cloudy* rounds the logarithm of the radial distance (and $\log \rho$ as well) to the third decimal number. This means that if the the sampling is too fine, the resulting radial distances may be read as equal. The radius in the input density profile have to be strictly increasing (for obvious reasons), henceforth a control is required on the radial array.

The adopted principle is quite simple: once all the points have been determined by the adaptive radius routine, another routine controls the distance between two points of $\log r$, starting from the beginning of the sorted array. If the distance is greater than a certain tolerance (in our case $tol = 0.00001$), the second point is removed and the process starts again.

In the end the spacing between all the point will be greater than the tolerance, so that the rounding performed by *Cloudy* will produce a strictly increasing array. If the number of points still exceeds 500, random points will be popped from the array until the requirements are met.

Chapter 3

Example of Model creation

In this chapter we provide a step-by-step introduction to PCG in the form of a commented PYTHON notebook. This process allows to generate a 2D model of ENLR, however some functions lack the complete list of input parameters for reasons of space. We refer to section 2.3 for a full documentation.

To begin with the model creation we import the basic needed libraries:*os* to access to bash commands in python, *numpy* for math and array manipulation, *matplotlib* for the plots, *pyCloudy* to interact with *Cloudy* and finally *clouds* are the libraries composing the Procedural Cloud Generator. All the PCG functions will be called with `nubi.function()`.

```
In [1]: %matplotlib inline
        import os
        import numpy as np
        import matplotlib.pyplot as plt
        import pyCloudy as pc
        import clouds as nubi
```

The output folder is created. This folder will contain the PCG output files: the torus and disk files, containing all the clouds of the two objects, and the reduced files produced by `check_clouds`.

```
In [2]: dir_ = '/home/path/to/twodmaps/twod_out/'
        os.mkdir(dir_)
```

```
In [3]: torus_file = dir_ + 'torus'
        disk_file = dir_ + 'disk'
```

In the next step we proceed to define the torus object. Given that the internal boundary of the torus is determined by the AGN luminosity, in this step we also define the main parameters of the system: M_{BH} and η, the Eddington ratio. The cloud density distribution parameters μ_d and σ_d are the same as in equation 2.3.

```
In [4]: #torus geometry
        M_BH = 10**9
        L_edd = 1.5*10**38 * M_BH
        Edd_ratio = 0.01
        L_agn = Edd_ratio * L_edd
        L_agn_sol = L_agn/nubi.L_sun
        R_sub = 0.47*(L_agn/(10**46))**(0.5)
        R_in = R_sub*nubi.parsec
        R_out = 170 * R_in
        opening =  100
        atm_thick = 10


        # cloud density distribution torus
        dens_mu_t = 10.
        dens_sigma_t = 0.3
        diff_dens_t = 1000.
        ff_t = 0.1


        den_dist_t = np.random.lognormal(...)


        cl_rad_t = 0.3*nubi.parsec
        cl_volume_t =(4/3.)* np.pi*(cl_rad_t**3)
        cl_mass_t = den_dist_t*cl_volume_t
        mass_spec_t = [1]
        torus = nubi.torus(R_in,R_out,opening,ff_t,...)
        torus.print_properties()
```

```
Torus properties
 R_in:5.61686560302e+17
 R_out:9.54867152514e+19
 opening_angle:100
 filling_factor:0.1
 volume:1.53003341964e+60
 cloud_radius:9.25703273974e+17
 cloud_mass:[  4.31604235e+58    1.11952515e+59    4.12418020e+58 ...]
 cloud_volume:3.32279852081e+54
 n_clouds:46046
 slope:0.839099631177
 atm_thickness:10.0 deg
```
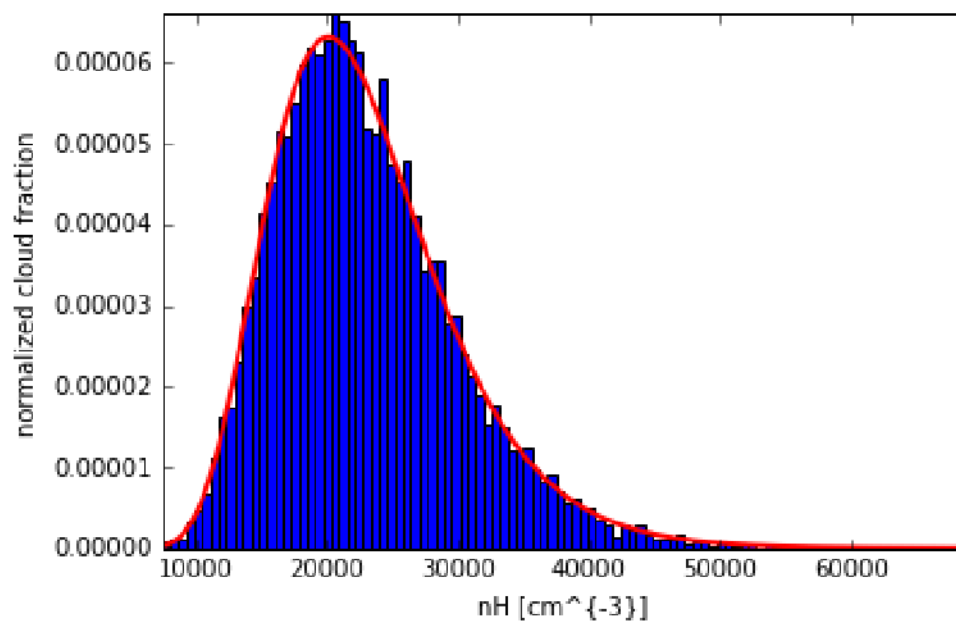
Below we plot the density distribution of the clouds generated in the torus. It is a useful check to be sure that the cloud densities respond to the user will.

In [5]: nubi.plot_dens_distrib(den_dist_t,dens_mu_t,dens_sigma_t)
        plt.savefig('t_dens_dist.jpg',dpi=200)

Once all the torus parameters are defined we can start the cloud generation. A text file containing the center coordinates, radii and masses of all the clouds will be created in the chosen directory.

After the generation we printed, as a sanity check, $\log_{10} M_T/M_\odot$, where M_T is the torus total mass.

In [6]: torus.gen_clouds(mass_profile = 'lognorm',distribution='zgaussian')
        print np.log10(nubi.total_cloud_mass(torus_file))

6.46785325813

In [7]: r_max = 10**3 * nubi.parsec
        nubi.plot_torus_sidecut(torus_file,R_in,r_max)
        plt.savefig('torus_sidecut.jpg',dpi=200)
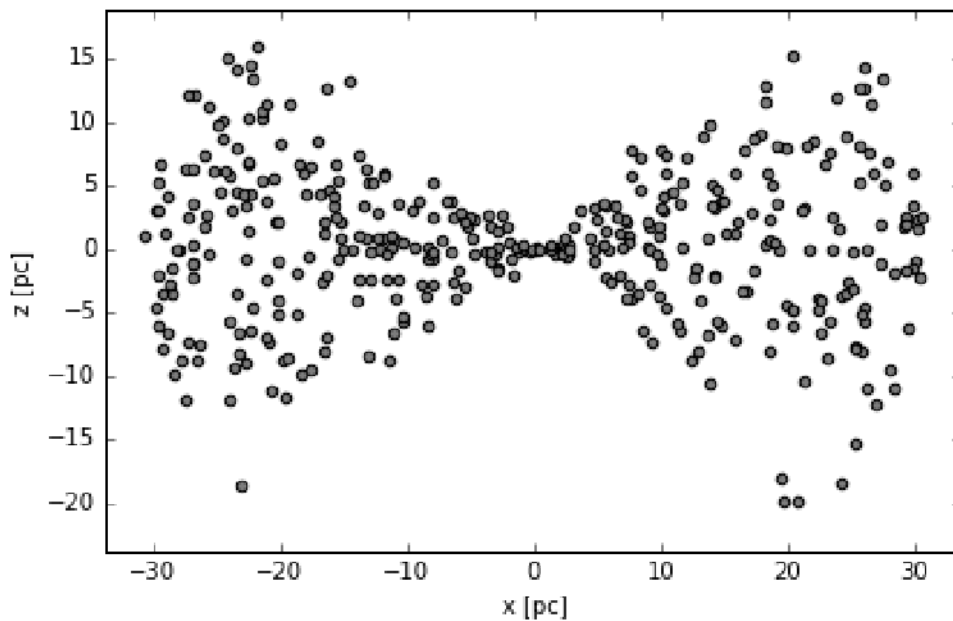
Now the angles of the model are defined. As we stressed in chapter 2 the bidimensional models are realized through several one-dimensional radial models, hence we have to choose the directions along which *Cloudy* will run. For this example we chose to leave $\phi = 0$ and sample over θ every 10 degrees.

```
In [8]: thetas = np.linspace(0.0,np.pi/2.,10)
        phi= 0.0
```

The next step is to create reduced files for each angle through the `check_clouds` routine (see section 2.3.7). The routine will print the number of clouds found in each angle.

```
In [9]: for theta in thetas:
            nubi.check_clouds(torus_file,theta,phi,verbose=True)
```

```
found 0 clouds in angles theta:0.0 phi:0.0
found 0 clouds in angles theta:10.0 phi:0.0
found 0 clouds in angles theta:20.0 phi:0.0
found 0 clouds in angles theta:30.0 phi:0.0
found 0 clouds in angles theta:40.0 phi:0.0
found 2 clouds in angles theta:50.0 phi:0.0
found 6 clouds in angles theta:60.0 phi:0.0
found 14 clouds in angles theta:70.0 phi:0.0
found 17 clouds in angles theta:80.0 phi:0.0
found 18 clouds in angles theta:90.0 phi:0.0
```

The adaptive radial sampling defines the radius array for each angle. However it only adds points when it finds a cloud and a full radial coverage of the gas distribution is needed. For this reason we add a base radius with a limited amount of points but covering the whole range of distances. In this case we are only sampling over the torus to calculate the column densities, so the base radius goes from R_{in} to R_{out}. The points obtained by the `adaptive_radius` routine will then be added to the base radius and sorted in ascending order.

```
In [10]: newfiles=[]
         rs = []
         base_start = np.log10(R_in)
         base_stop =np.log10(R_out)
         base_radius = np.logspace(base_start,base_stop,100)
         for thet in thetas:
```

```python
        dtfiles= [torus_file+'_ridotto_{0:.2f}_0.00'.format(...)]
        newfiles.append(dtfiles)
        r = nubi.adaptive_radius(dtfiles,thet,phi,7,3)
        r = np.concatenate((r,base_radius))
        r = np.sort(r)
        rs.append(r)
```

The next step retrieves the density profile summing the cloud densities with
the diffuse density profile. At the end of this cycle we obtain the torus column
densities. These are useful indicators of the consistency of the model.

```python
In [11]: densities = []
        col_densities = []


        for thet,r,f in zip(thetas,rs,newfiles):
            rho = nubi.get_density_general(f,r,thet,0.0)
            rho = torus.get_diffuse_profile(r,rho,thet,profile = 'gaussian')
            densities.append(rho)
            col_dens = nubi.column_density(rho,r)
            col_densities.append(col_dens)
            log_r = np.log10(r)
            log_rho = np.log10(rho)


        print 'Mean column density {0}'.format()
        print 'Median column density {0}'.format()
        print 'Minimum column density {0}'.format()
        print 'Maximum column density {0}'.format()
```

```
Mean column density 23.319820471
Median column density 22.9653651682
Minimum column density 10.1864764357
Maximum column density 23.8559344672
```

Once we are satisfied with the torus we can proceed and generate the disk. While the process is similar we should take care in the orientation of the disk. Leaving $\alpha = 0$ the minor axis of the disk will be coincident with the torus axis, meaning that less gas would be available to be ionized.

```
In [12]: #disk geometry
         inner_radius = R_out
         major = 10**4 * nubi.parsec
         minor = 10**3 * nubi.parsec
         alpha = 90.


         # cloud density distribution disk
         dens_mu_d = 4.
         dens_sigma_d = 0.6
         diff_dens_d = 10**(-2)
         ff_d = 0.02
         den_dist_d = np.random.lognormal(...)

         cl_rad_d = 30*nubi.parsec
         cl_volume_d =(4/3.)* np.pi*(cl_rad_d**3)

         cl_mass_d = den_dist_d*cl_volume_d
         mass_spec_d = [1]

         disk = nubi.disk(major,minor,inner_radius,alpha, ff_d,...)
```

```
Disk properties
 major:3.08567757991e+22
 minor:3.08567757991e+21
 inner:9.54867152514e+19
 filling_factor:0.02
 volume:1.23066575414e+67
 cloud_radius:9.25703273974e+19
```

```
cloud_mass:[   1.52625088e+62    1.82717564e+62    8.08932842e+61 ...]
cloud_volume:3.32279852081e+60
n_clouds:74074
```

```
In [13]: nubi.plot_dens_distrib(den_dist_d,dens_mu_d,dens_sigma_d)
         plt.savefig('disk_dens_dist.jpg',dpi=200)
```
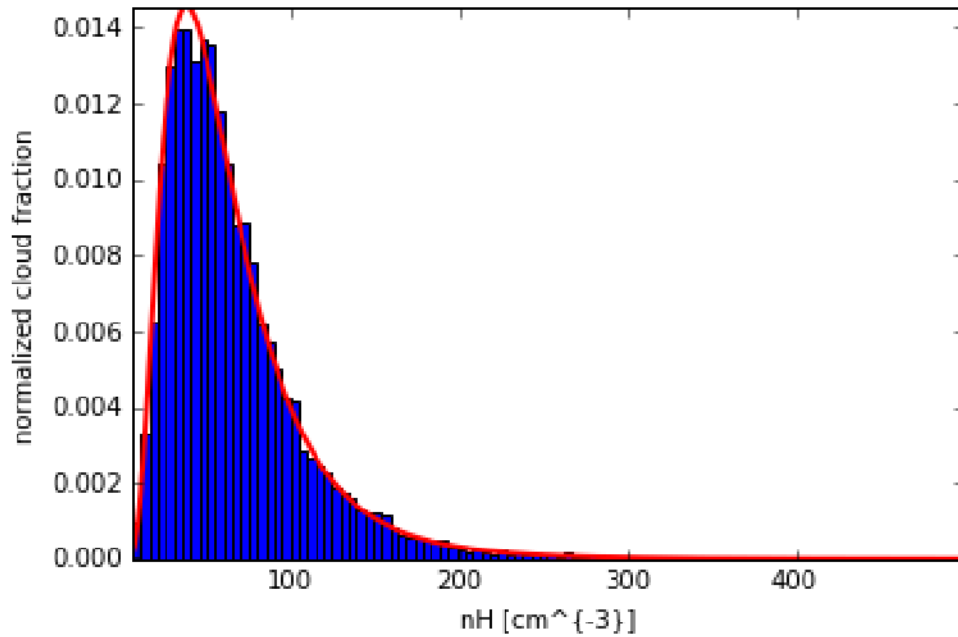

Again, once we are satisfied with the disk parameters we can start the generation.

```
In [14]: disk.gen_clouds()
         print np.log10(nubi.total_cloud_mass(disk_file))
```

```
10.130850372
```

```
In [15]: nubi.plot_clouds_cut(disk_file,major)
         plt.savefig('disk_cl_dist.jpg',dpi=200)
```

```
Retrieving cloud positions
```
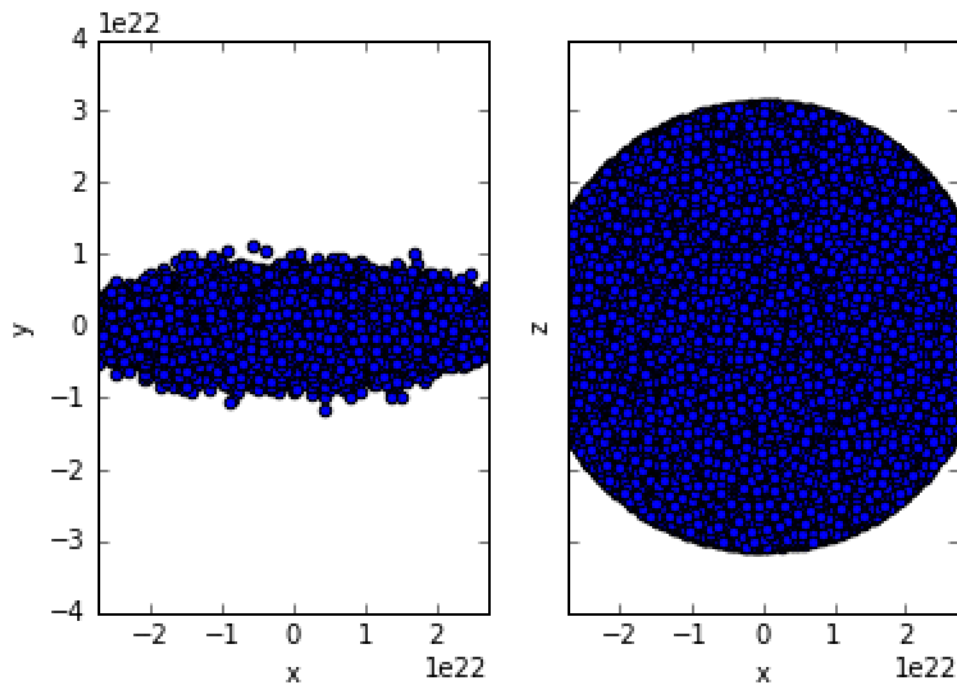
As before we need to identify the clouds intersected by our lines:

```
In [16]: for theta in thetas:
             nubi.check_clouds(disk_file,theta,phi,verbose=True)
```

```
found 4 clouds in angles theta:0.0 phi:0.0
found 3 clouds in angles theta:10.0 phi:0.0
found 3 clouds in angles theta:20.0 phi:0.0
found 8 clouds in angles theta:30.0 phi:0.0
found 2 clouds in angles theta:40.0 phi:0.0
found 4 clouds in angles theta:50.0 phi:0.0
found 7 clouds in angles theta:60.0 phi:0.0
found 6 clouds in angles theta:70.0 phi:0.0
found 7 clouds in angles theta:80.0 phi:0.0
found 9 clouds in angles theta:90.0 phi:0.0
```

Now the whole density profile is calculated, taking both into account the disk and the torus. The first step is the adaptive radial sampling:

```python
In [17]: old_rs = []
         newfiles= []
         base_start = np.log10(R_in)
         base_stop =np.log10(major)
         base_radius = np.logspace(base_start,base_stop,100)
         for thet in thetas:
             dtfiles= [torus_file,disk_file]
             newfiles.append(dtfiles)
             r = nubi.adaptive_radius(dtfiles,thet,0,9,3)
             r = np.concatenate((r,base_radius))
             r = np.sort(r)
             old_rs.append(r)
```

This time we run the `check_and_remove` routine to be sure that the maximum array length is 498. A total of 500 pairs is permitted but we leave two spaces free in case it is necessary to add a point at the beginning or the end.

```python
In [18]: rs=[]
         for r in old_rs:
             r = nubi.check_and_remove(r,0.0001,498)
             rs.append(r)
```

```python
In [19]: densities = []
         col_densities = []

         for thet,r,f in zip(thetas,rs,newfiles):
             rho = nubi.get_density_general(f,r,thet,0.0)
             rho = torus.get_diffuse_profile(r,rho,thet,...)
             rho = disk.get_diffuse_profile(r,rho,thet,...)
             densities.append(rho)
             col_dens = nubi.column_density(rho,r)
             col_densities.append(col_dens)
```

```
        print 'Mean column density {0}'.format()
        print 'Median column density {0}'.format()
        print 'Minimum column density {0}'.format()
        print 'Maximum column density {0}'.format()
```

```
Mean column density 23.4298017146
Median column density 23.1454633508
Minimum column density 22.3057041944
Maximum column density 23.914702976
```

Now the *Cloudy* input files can be written. With the first array `emis_tab` we define which spectral line emissivities will be saved at each zone of the calculation. It is important to define beforehand the lines because otherwise only the emissivities emerging from the far side of the cloud will be available. The options are all those commands that are not included in the pyCloudy libraries. In our case these are CMB (it adds the CMB background to the calculations, it is not relevant but otherwise *Cloudy* will complain) and the grain option to include dust (see appendix A).

```
In [20]: def set_models(dir_, model_name):
            emis_tab = ['H  1  4861',
                        'H  1  6563',
                        'He 1  5876',
                        'N  2  6584',
                        'O  1  6300',
                        'O II  3726',
                        'O II  3729',
                        'O  3  5007',
                        'TOTL  4363',
                        'TOTL  4861',
                        'S II  6716',
                        'S II  6731'
                        ]
```

```python
        options = ['CMB','grains ism function sublimation']
        model = pc.CloudyInput()
        model.set_emis_tab(emis_tab)
        model.set_abund(predef = 'ism')
        model.set_star(SED = 'agn', SED_params)


        for theta,r,rho in zip(thetas,rs,densities):
            model.set_other()
            rs_in = np.log10(r[0])+0.01
            model.set_radius(rs_in)
            densitystring = nubi.denstostring(r,rho,depth=False)
            model.model_name = '{0}/{1}_ff{2}_dd{3}_theta-{4:.3f}'
            model.set_other(options)
            model.set_other(other_str = densitystring)
            model.set_theta_phi(theta*180/np.pi,phi*180/np.pi)
            model.set_iterate(to_convergence = True)
            model.print_input(to_file = True, verbose = False)
```

```python
In [21]: dir_toc='/home/path/to/twodmaps/example_to_cloudy/'
         os.mkdir(dir_toc)

In [22]: model_name = 'example'
         set_models(dir_toc,model_name)
```

Chapter 4

Photo-ionization models of a clumpy medium

In this chapter we present two sets of models realized with PCG: composite cloud models and an extended multi-component medium. For the moment we do not take into consideration spatial effects induced by the torus but only the ionization of gas in the ENLR. The aim is to reproduce what emerges from one-zone and two-zone models with this new approach.

The first set of models, that we named composite cloud models, is intended to describe the ionization in an ionization-bounded cloud composed of several smaller overdensities surrounded by a lower density gas.

The second set is composed of radial models where the clouds are, as a first approximation the only source of gas in the modeled space, in other words the diffuse component density is extremely low.

4.1   Composite clouds

The region of gas in composite cloud models is modeled through the cone object described in section 2.3.6. The cone initialization parameters are the same for the five models and are listed in table 4.1. The clouds are placed at 1 kpc from the source and the radiation is supposed to reach them unabsorbed.

The difference between the models lies in the cloud mass distribution. The chosen distribution is lognormal (see equation (2.3)) and five different values of μ_d

Parameter	Value
h_{in}	10^3 pc
h_{out}	10^4 pc
β	$20°$
ϕ_c	0.03
ρ_{diff}	$50\,\mathrm{cm}^{-3}$
r_{cl}	30 pc
μ_d	4,6,7,8,9

Table 4.1: Cone parameters of all the composite cloud models.

are considered: $\mu = [4, 6, 7, 8, 9]$ with fixed $\sigma_d = 0.6$. An example of the resulting distribution for $\mu = 6$ can be seen in figure 4.1. The considerable extent of the cone is meant only to avoid a fixed boundary for the cloud, that is the resulting depth will be determined by the gas ionization, or in other words the cloud is ionization bounded. In practice we created a cloud composed of several smaller clouds acting as local overdensities in a diffuse medium with $\rho_{diff} = 50\,\mathrm{cm}^{-3}$.

A total of 48 different angles were selected, picked from a uniform distribution
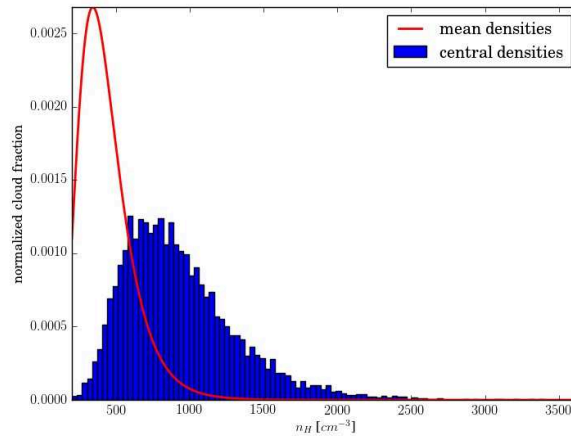

Figure 4.1: Numeric fraction of clouds with given density. The red line is the probability distribution function of the clouds mean density, while the blue histogram is the actual, binned, distribution of clouds central densities.

covering the whole cone. At the end of the calculation the maximum extent of the composite clouds, as determined by the maximum radius reached by *Cloudy*, was $\sim 100\,pc$. With an angular resolution of ~ 1 arcsec we can resolve spatially a

region of $\sim 200\,pc$ in a galaxy at a redshift $z = 0.015$. Therefore we can assume that the cloud emission would be unresolved if observed from Earth. All the line emissivities were integrated in radial and angular direction. It should be noticed that the line emission is a local emissivity $[\mathrm{erg\,cm^{-3}\,s^{-1}}]$, for this reason we will treat mainly emission line ratios.

In figure 4.2 the integrated line ratios are plotted in the three standard BPT-VO diagnostic diagrams. It is immediately evident how only the two models with $\mu_d = 4 - 6$ are in agreement with the emission of ionized gas typical of the ENLR in Seyfert galaxies. As the density grows, the lower ionization degree places the models outside the Seyfert region, in the LINERs zone or even below the AGN-H II separation line. This should not be interpreted as if the cause of the low ionization typical of LINERs is the high density of the gas; the high densities involved are implausible when considering the whole emission of a LINER galaxy. Locally, however, a high density cloud could mimic the LINER ionization due to the enhanced contribution of low-ionization lines such as [NII]$\lambda6584$ and [SII]$\lambda\lambda6717\,6731$.
The two higher density models have central cloud densities reaching value of $n_H \sim 1 - 5 \times 10^4\,cm^{-3}$. These values are not observed in ENLR, however is interesting to note how the emission line ratios for these models are degenerate and outside the AGN ionization zone.

4.2 Radial ionization in a multi-component medium

These models are realized in a similar fashion to the composite clouds. The distance of the cone is lower, however the gas is still placed farther than $500\,pc$ from the source. The main difference is in the densities involved. Lowering the contribution of the diffuse gas to $10^{-2}\,cm^{-3}$ the radiation is able to reach the denser clouds practically unabsorbed, and can travel thousand of parsecs before ionizing a cloud. Furthermore the cloud densities themselves are lower than the previous case, allowing us to model the radial ionization of the gas in the ENLR. The resulting ionization extends up to 10 kpc, however we considered a maximum
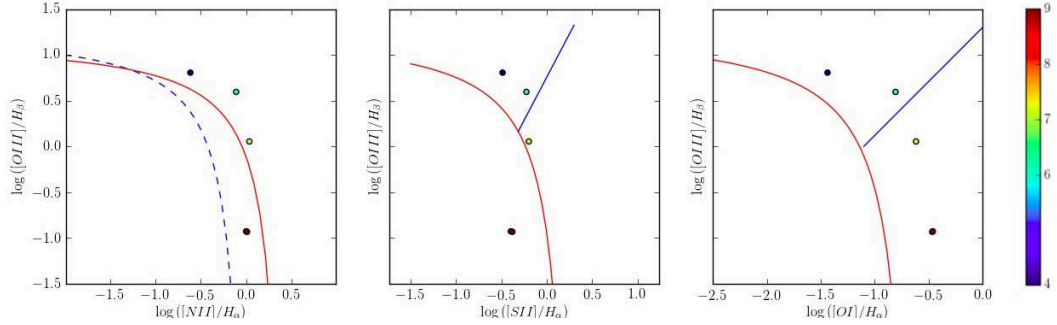
Figure 4.2: BPT diagnostic diagrams of the composite clouds models. Points are coloured on the basis of their logarithmic mean density μ. The red line (Kewley et al., 2001) in the three panels separates the emission of gas ionized by AGN (above the red line) from the ionization typical of H II regions. Below the blue dashed line (Kauffmann et al., 2003) in the left panel lies the zone of pure starburst. The blu solid line separates Seyfert-like emission from LINERs (Kewley et al., 2006).

distance equal to to the shortest extension between the models identified by the various angles. The emissivities have been binned in radial direction with 100 bins. The emissivities of each line are integrated in the bin and the associated radius is its mean value inside the bin. Due to the uneven spacing of the slab depths calculated by *Cloudy*, the bin dimensions are not fixed. In practice this means that the maximum radius reported in these radial models underestimates their true extension.

We obtained radial ionization sequences in the BPT diagrams, similar to those obtained through a single-zone model with varying ionization parameter. The ionization sequences are strikingly similar and proceed from the upper-left corner of the diagram, where the ionization is extremely high, to the lower right in the LINER region. The difference between the models is in the distance at which the ionization degree falls below the Kewley et al. (2006) line.

4.2.1   A note on He II

The HeII/H_{β} ratio is a critical feature in photo-ionization models (see section 1.4). Single-zone models tend to under-predict this ratio by a factor of 10. This issue has been solved with the introduction of two-zone models. These ad hoc
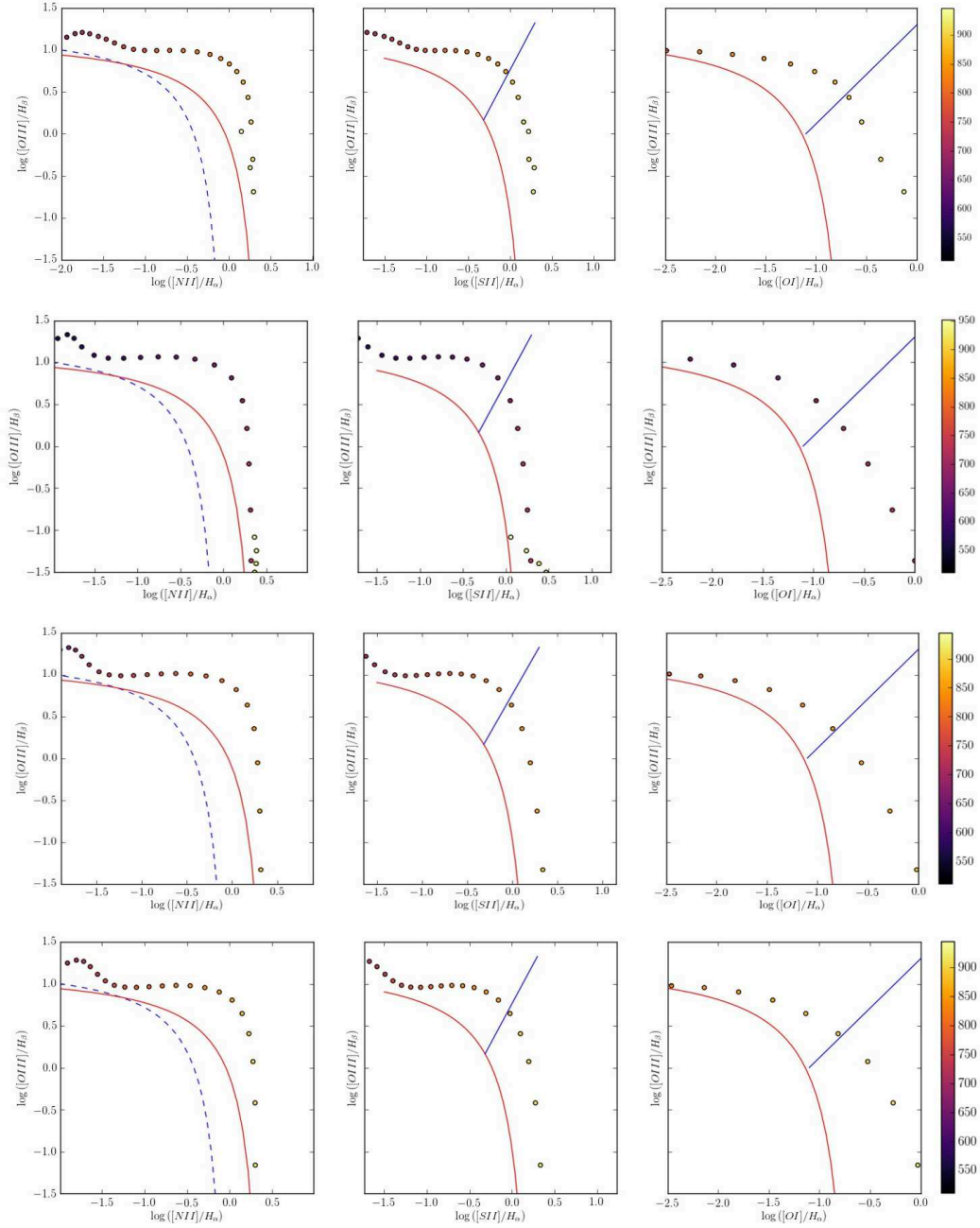
Figure 4.3: Radial ionization sequences of the four different models (see table 4.2). Density increases from the top row to the bottom one. Color bar units are parsec.

Parameter	Value
h_{in}	$5 \times 10^2 \, pc$
$h_o ut$	$10^4 \, pc$
β	$20°$
ϕ_c	0.03
ρ_{diff}	$10^{-2} \, cm^{-3}$
r_{cl}	$30 \, pc$
μ_d	$4, 4.5, 5, 5.5$

Table 4.2: Cone parameters of the multi-component medium.

models are able to reproduce the observed ratio (~ 0.3) with the right choice of parameters. From figure 4.4 we can see how, without imposing any particular condition we reduced the under-prediction to a factor 3 without any dependence on the model density.
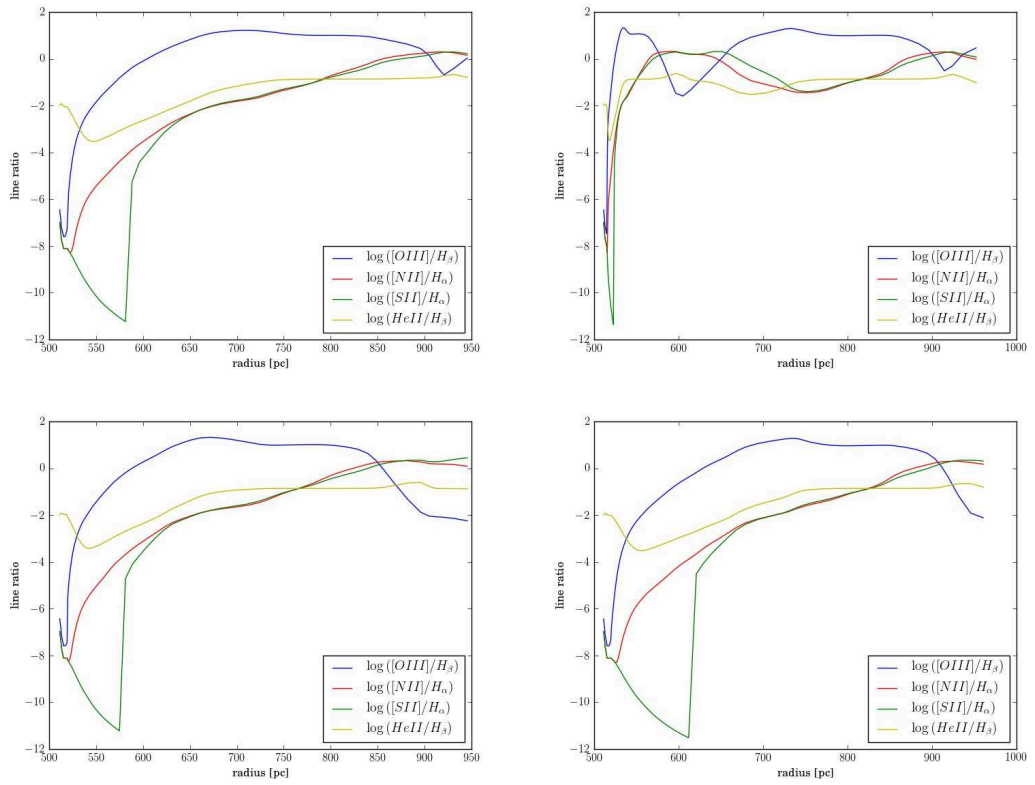

Figure 4.4: Caption

Chapter 5

Bi-dimensional models

In this chapter we show an example of what kind of bi-dimensional models is realizable with PCG. Bi-dimensional models are inherently time consuming: leaving aside the model construction that requires a few minutes, the calculations for a single angle can take up to 20 hours to converge. This means that running 64 angles on 8 cpu can take three days. It is immediately clear that realizing more complete 3D models would require more computational power and parallel computing. For this reason the 2D maps we realized represent only a slice of the emission in the ENLR. The dark areas in the [O III]/H$_\beta$ maps below (see top left panels of figures 5.1, 5.2, 5.3 and 5.4) are caused by the early absorption of the ionizing radiation by clouds close to the AGN. In a real case the emission would come from clouds placed on different planes where the radiation can reach them undisturbed. Anyway these maps provide a good representation of the line ratios in the ENLR.

5.1 Model construction

All the four models presented below are constructed with a torus plus disk configuration. The disk minor axis is perpendicular to the torus axis, this means that the escaping radiation has plenty of gas clouds to ionize in the disk plane. The first three models differ only on the torus filling factor while the fourth is intended to test a different gas distribution in the disk. The parameters of the the different models are shown in table 5.1.

The chosen ionization source is an AGN SED as presented in section 2.3.3, with a bolometric luminosity derived from a BH mass of $10^9\, M_\odot$ and an Eddington ratio $\eta = 0.01$. These are common values for a Seyfert galaxy and result in a luminosity $L_{AGN} \sim 10^{45}\, \mathrm{erg\, s^{-1}}$.

The dusty torus is clumpy and has the same structure and extension in all the models. Its opening angle is set to $100°$ and the inner and outer boundaries depend on the AGN luminosity. The smooth component of the gas distribution is Gaussian-like (see equation 2.6) with higher density towards the torus plane. The galactic disk is generated with the same parameters for all the models with exception of the fourth model in which it is compressed in a much thinner ellipsoid with minor axis $b = 10^2\, \mathrm{pc}$. While in principle reducing the disk thickness should not impact on the results (the cloud number density is still the same), we will see that it has a minor impact on the [OIII]/H$_\beta$ ratio. The extension of the disk is 10 kpc in order to provide enough gas to be ionized by the AGN without weighting too much on the model construction time.

Parameter	Torus	Disk
Inner boundary	$R_{in,T} \sim 0.1$ pc	$R_{out,T}$
Outer boundary	$R_{out,T} = 170\, R_{in,T}$	$a = 10^4$ pc , $b = 10^3$ pc
Opening and incl.	$\xi_{oa} = 100°$	$\alpha_{inc} = 90°$
ϕ	0.05, 0.08, 0.1	0.02
ρ_{diff}	$10^3\, \mathrm{cm^{-3}}$	$10^{-2}\, \mathrm{cm^{-3}}$
r_{cl}	0.5 pc	30 pc
μ_d	9	4

Table 5.1: Disk and torus parameters of the 2D models.

5.2   Bi-dimensional ionization maps

For each of the four models we realized emission line ratio maps. We covered the canonical line ratios of diagnostic diagrams: [OIII]/H$_\beta$, [NII]/H$_\alpha$, [OI]/H$_\alpha$ and [SII]/H$_\alpha$. Moreover following section 4.2.1 we created He II/H$_\beta$ maps to confirm the results of the previous chapter.

Each map represents an area of 2×2kpc with the ionizing source placed in the bottom left corner. From this corner a solid red line is traced and it represents the projection of the torus edge, the torus clumps are generated below this line in

a region of ~ 10 pc close to the bottom left corner. Conversely the blue dashed line represents the projection of the torus atmosphere, the limit above which the diffuse gas component of the torus becomes negligible.

As we can see from the top left panel of figures 5.1, 5.2, 5.3 and 5.4 the highest values of [OIII]/H$_\beta$ lie almost entirely above the red line, marking the ionization cone. The values of the [OIII]/H$_\beta$ ratio are consistent with typical AGN values (e.g. Kewley et al. 2006) and have little variations between the different models. This should be expected given that the parameters of the generated gas distribution are the same for the four models. In principle one should expect that the edge of the torus (the red line) should sharply separate the two areas, however we also find high values of [OIII]/H$_\beta$ below the line. The cause of this behaviour lies in the clumpiness of the torus: radiation is likely filtering through the torus because there are not enough clumps to absorb it.

The large variations of these emission line ratios we can observe in each model tell us that local conditions of the gas, such as the distribution of clouds, has a large impact on what we observe.

5.2.1 Leaking radiation

As introduced in section 1.3.1, a handful of objects show signs of AGN ionization in the cross-cone region. A possible explanation could be that ionizing radiation leaks from the gaps between the clumps of the torus partially attenuated. These regions are characterized by lower values of [OIII]/H$_\beta$ with respect to the cone and conversely by values of low-ionization line ratios such as [NII]/H$_\alpha$, [OI]/H$_\alpha$ and [SII]/H$_\alpha$ similar to those inside the cone (see for instance figure 11 of Cracco et al. 2011). In the diagnostic diagrams these regions would fall close to the Seyfert-LINER separation line.

We realized three models with different torus filling factor to test if the torus clumpiness is a viable explanation for the cross-cone ionization. From figures 5.1, 5.2, 5.3 and 5.4 it is clear that radiation is indeed capable of leaking through the torus and ionize the gas in the cross-cone region while the absorption provided by the dusty clumps keeps the [OIII]/H$_\beta$ ratio to lower values compared to the cone. Moreover when the filling factor increases, and along with it the probability
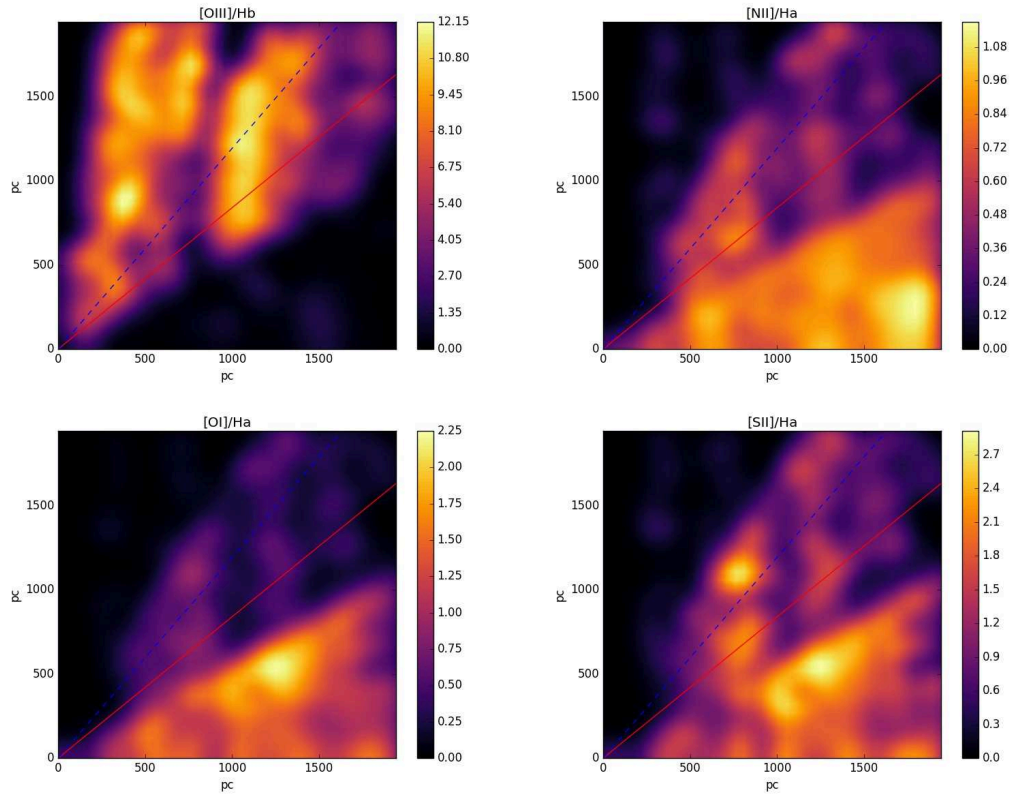
Torus filling factor 0.05

Figure 5.1: Line ratio maps of the $\phi_T = 0.05$ model. The source of ionization is placed at the bottom left corner of each panel, while the torus section lies on the x axis. The red solid line represents the projection of the edge of the torus. The blue dashed line is the projection of the torus atmosphere. The top left panel is the [O III]/H$_\beta$ map where is clearly visible how the ionization cone is created by the torus occultation.
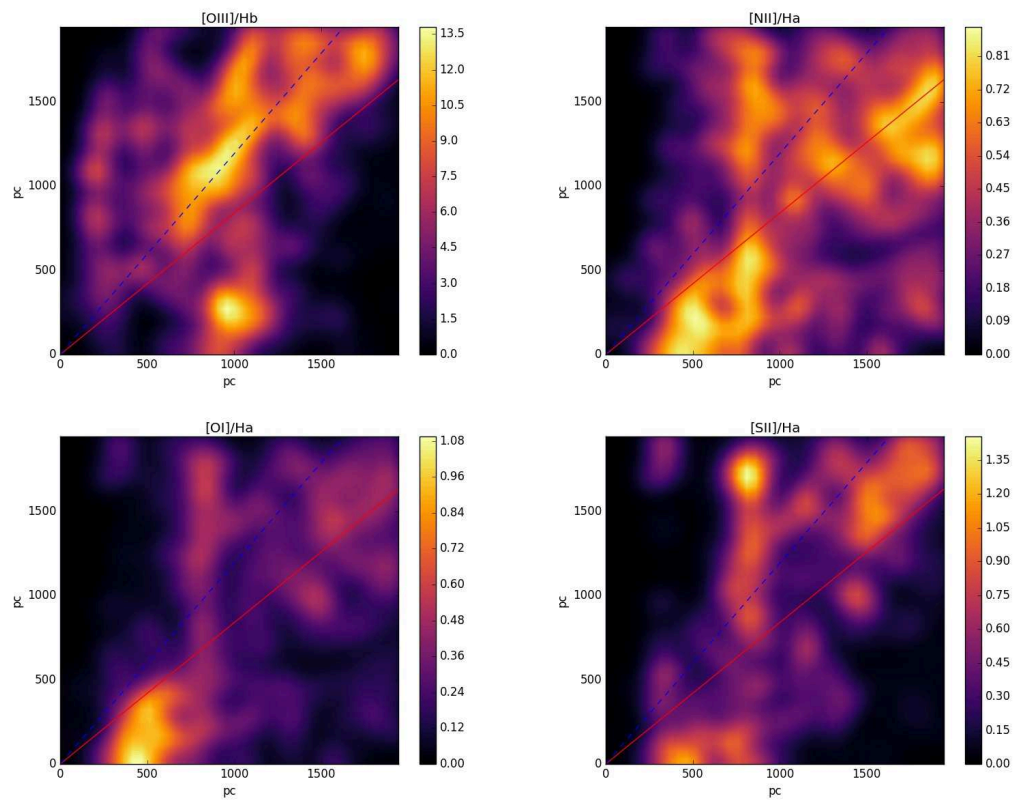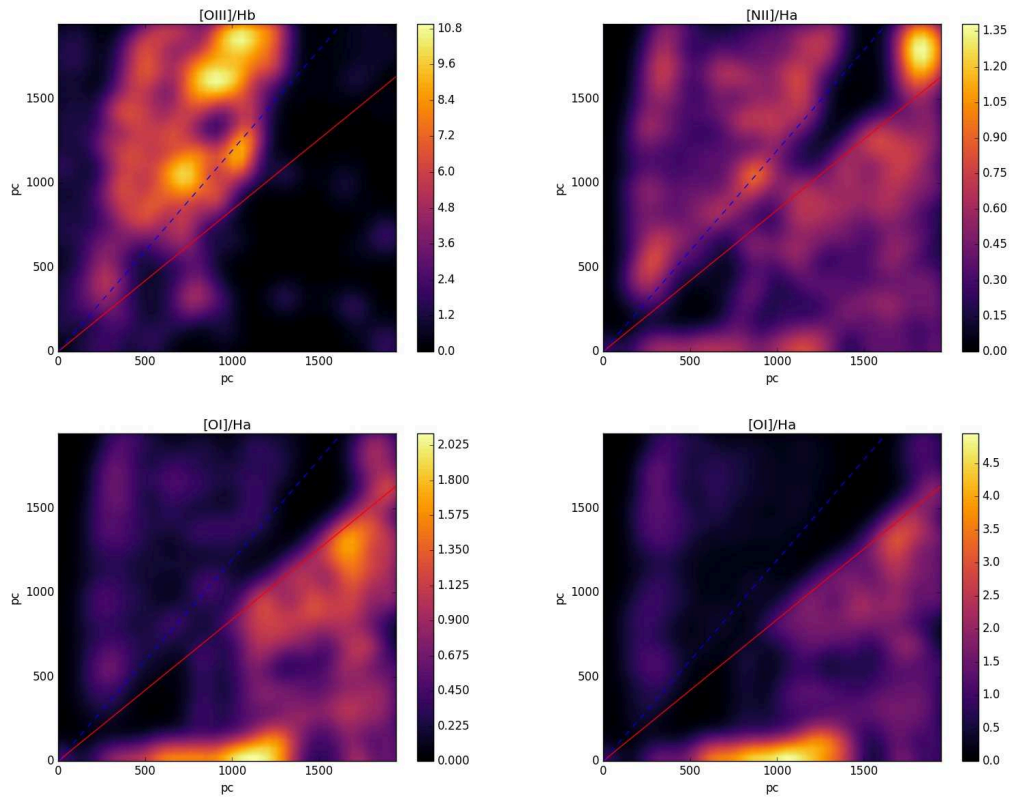
Figure 5.2: As in figure 5.1. The increased filling factor of the torus reduces the values of low-ionization emission line ratios

Torus filling factor 0.1

Figure 5.3: Emission line ratio maps as in figure 5.1 for the $\phi_T = 0.1$ model.

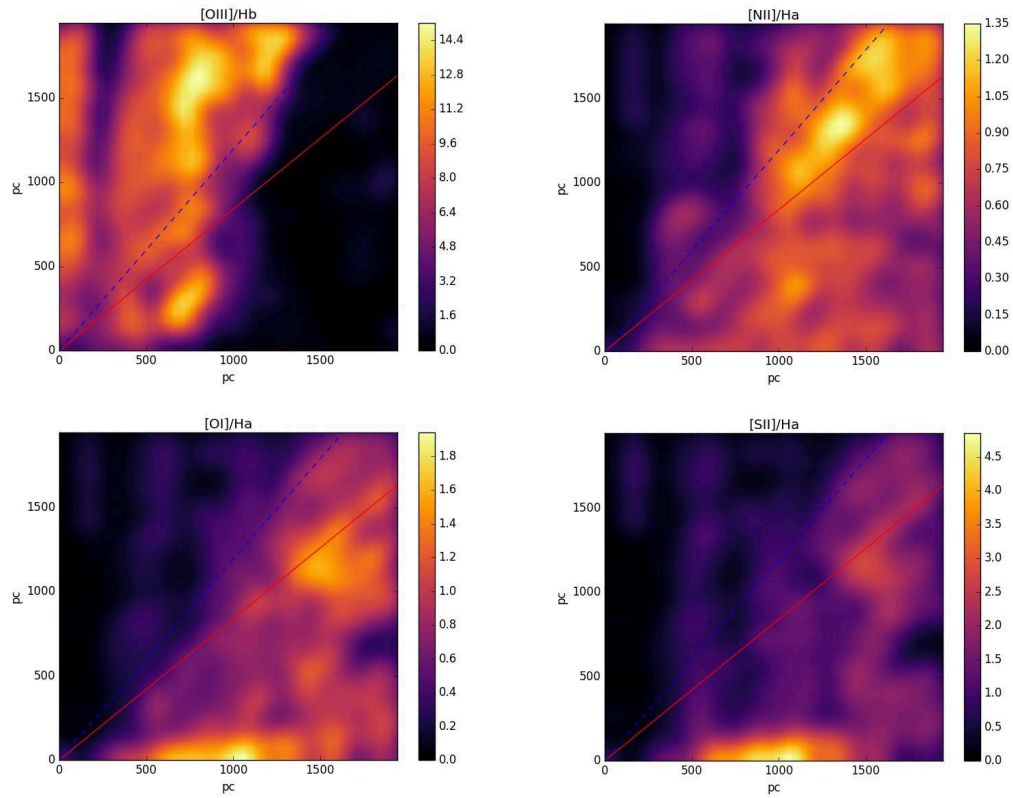**Torus filling factor 0.1 planar disk**

Figure 5.4: Same maps of 5.1. This model differs from the previous one only in the thickness of the gas disk. Even if the disk filling factor is the same, the clouds are more concentrated in the plane were the calculation are done. This causes a more uniform distribution of the emission, especially in the [OIII]/H$_\beta$ map.

of a photon to be absorbed, the gas becomes less ionized.

The observation of ionized gas in the cross-cone region seems compatible with radiation filtering through the torus. The peculiarity of each target however would require dedicated and more thorough models.

5.2.2   Another note on He II

The He II/H$_\beta$ ratio maps of the four different models are shown in figure 5.5. The bi-dimensional models under-predict the observed values by a factor of 3, just like the multi-cloud models of chapter 4. The interesting feature we can observe is that the presence of the torus seems not to be relevant, the value of HeII/H$_\beta$ has little changes between the cone and cross-cone region.
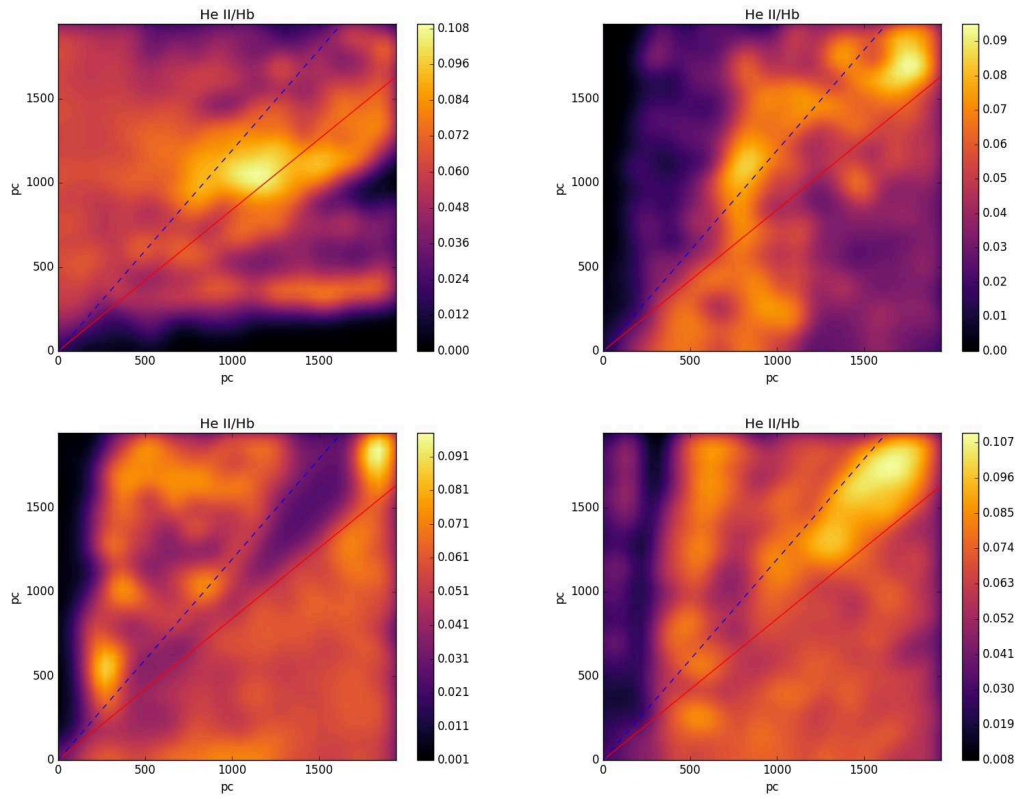

Figure 5.5: He II/H$_\beta$ maps for the four different models

Chapter 6

Conclusions

The aim of this thesis is to explore a new approach to photo-ionization models of extended gas regions in AGN, specifically the ENLR of Seyfert galaxies, able to address spatial effects, such as the footprint of the torus structure in the ionization of gas clouds several kpc away. This idea rises from the advent in the last decades of the integral field spectroscopy. The possibility to study the spectrum of ionized gas in different regions of a galaxy hosting an AGN could help to shed light on the characteristics of the torus, which prevents the isotropic escape of ionizing photons and creates spectacular ionization cones.

Due to the complexity of the subject and the large number of parameters involved, this kind of models is realized through dedicated radiative transfer code such as *Cloudy*. The first and most straightforward path to reproduce the observed optical features in AGN has been to compute the spectrum of a single cloud, ionized by a non-thermal continuum typical of AGN. The discrepancy between the observations and these simple models however has prompted the necessity of different populations of gas clouds, responsible of both high and low ionization emission lines in the NLR and ENLR.

The proposed new approach is intended to tackle both these issues by means of a three-dimensional distribution of gas, generated by the PCG code, that is used to provide the chosen photo-ionization code (*Cloudy* in our case) several one-dimensional gas density profiles. Each one of these profiles samples the gas distribution along different direction, in this way the outputs of *Cloudy* can be interpolated to create pseudo 2D and 3D maps of emission lines.

The Procedural Cloud Generator is a PYTHON code designed to interact with *Cloudy* and write its input files. It allows the user to:

1. Define the ionizing source in terms of BH mass and Eddington ratio, scaling the total luminosity of the spectral energy distribution.

2. Generate the torus choosing among various configurations: smooth, clumpy or composite. The extension of the torus automatically determined by the code depending on the AGN luminosity.

3. Define and create a disk of gas and populate it with clouds of different densities. The disk can be placed at a chosen inclination with respect to the torus axis.

4. Take advantage of this new approach to create "classical" models without the need to generate large distributions of gas, thanks to the cone object.

5. Calculate the density profile along every direction needed through the adaptive radial sampling technique.

6. Plot the outputs of *Cloudy* thanks to the integration with the pyCloudy libraries.

The resulting models performance is comparable to single-zone and two-zone models, adding as an advantage the possibility to realize bi-dimensional models and to study spatial effects in the ENLR. We proved this approach could be a viable option to explain cross-cone ionization in Seyfert galaxies, however further investigation is still needed. The potentiality of the PCG code does not end with AGN, it can be used in all scientific cases involving the ionization of a uneven distribution of gas. The main downside of this method is that the reliability depends heavily on the available computational time.

We can conclude that this new approach to ENLR models could help to give constraints to the torus structure in terms of its footprint on the ionized gas in the host galaxy. The processing power available to us, although appreciated, was not sufficient to fully take advantage of the code potential. Complete three-dimensional models would be the natural continuation of this work.

Appendix A

Cloudy abundances and grains

The choice of the chemical mixture of the gas is often critical in the construction of suitable models. *Cloudy* offers a vast number of pre-defined sets of abundances and the possibility to tune the contribution of specific elements or define a completely new set. Abundances are always specified by number relative to the total hydrogen density and refer only to the gaseous phase, meaning that they do not account for elements locked in dust grains.

A.1   Gas abundances

If the `abundances` command is not specified the default chemical composition is solar. The stored chemical compositions can be modified, for instance by scaling the abundance of a single element by a chosen factor. We report below a brief summary of the stored abundances along with the due references. The values of each set are shown in table A.1. Some of the stored sets come with associated grain abundances.

Solar

It is the default composition. Carbon and oxygen abundances come from photospheric abundances of Allende Prieto et al. (2001, 2002),while N, Ne, Mg and Fe are from Holweger (2001). The remaining elements come from Grevesse & Sauval (1998).

H II region

These abundances come from a mean of the Orion Nebula abundances determined by Baldwin et al. (1991), Rubin et al. 1991, Osterbrock et al. 1992, Rubin et al. 1993, while the grain size distribution comes from Baldwin et al. (1991).

Planetary

Chemical composition of a typical planetary nebula. Values are from Aller & Czyzak (1983) and Khromov (1989).

Nova

The values are those derived by Ferland & Shields (1978) for the classical nova V1500 Cygni.

Cameron

Abundances from Cameron (1982). The helium abundance is very low and incompatible with the Big Bang.

Primordial

Primordial abundances from the cosmological nucleosynthesis.

ISM

The gas-phase abundances are an average from the work of Cowie & Songaila (1986) for the warm and cold phases of the ISM combined with values from Savage & Sembach (1996).The oxygen abundance is from is from Meyer et al. (1998), F is from Snow et al. (2007) and Co is from Mullman et al. (1998). The dust is composed by interstellar medium grains defined by Mathis et al. (1977).

Crab

These values for the Crab Nebula are from model M1 of Pequignot & Dennefeld (1983).

A.2   Dust

The dust treatment is included by default when choosing H II region, ISM or planetary nebula. In these cases, elements like Si, Ca, Al, Mg and Fe are heavily depleted onto dust grains. In the ISM case, which we used throughout this work, the size distribution and abundances of grains are appropriate for the ISM of our galaxy. This includes both graphite and silicate components and reproduces the extinction properties for a ratio of extinction per reddening of $R_V \equiv A_\nu / E(B - V) = 3.1$.

	Atom	Solar	H II region	Planetary	Nova	Cameron	Primordial	ISM	Crab
1	H	1.00E+00	1.00E+00	1.00E+00	1.00E+00	1.00E+00	1.00E+00	1.00E+00	1.00E+00
2	He	1.00E-01	9.50E-02	1.00E-01	9.8E-02	6.77E-02	7.20E-02	9.80E-02	7.00E-01
3	Li	2.04E-09	5.40E-11	1.00E-20	2.05E-09	2.20E-09	1.00E-10	5.40E-11	-
4	Be	2.63E-11	1.00E-20	1.00E-20	2.62E-11	4.50E-11	1.00E-16	1.00E-20	-
5	B	6.17E-10	8.90E-11	1.00E-20	7.60E-10	3.40E-10	-	8.90E-11	-
6	C	2.45E-04	3.00E-04	7.80E-04	9.40E-03	4.22E-04	-	2.51E-04	7.00E-03
7	N	8.51E-05	7.00E-05	1.80E-04	9.80E-03	8.72E-05	-	7.94E-05	1.23E-04
8	O	4.90E-04	4.00E-04	4.40E-04	1.70E-02	6.93E-04	-	3.19E-04	1.70E-03
9	F	3.02E-08	1.00E-20	3.00E-07	3.02E-08	2.90E-08	-	2.00E-08	-
10	Ne	1.00E-04	6.00E-05	1.10E-04	2.03E-03	9.77E-05	-	1.23E-04	5.33E-04
11	Na	2.14E-06	3.00E-07	1.90E-06	2.06E-06	2.25E-06	-	3.16E-07	-
12	Mg	3.47E-05	3.00E-06	1.60E-06	3.80E-05	3.98E-05	-	1.26E-05	8.00E-05
13	Al	2.95E-06	2.00E-07	2.70E-07	2.95E-06	3.20E-06	-	7.94E-08	-
14	Si	3.47E-05	4.00E-06	1.00E-05	3.55E-05	3.76E-05	-	3.16E-06	-
15	P	3.20E-07	1.60E-07	2.00E-07	3.73E-07	3.72E-07	-	1.60E-07	-
16	S	1.84E-05	1.00E-05	1.00E-05	1.62E-05	1.88E-05	-	3.24E-05	3.5E-05
17	Cl	1.91E-07	1.10E-08	1.70E-07	1.88E-07	1.78E-07	-	1.00E-07	-
18	Ar	2.51E-06	3.00E-06	2.70E-06	3.63E-06	3.99E-06	-	2.82E-06	-
19	K	1.32E-07	1.10E-08	1.20E-07	1.35E-07	1.35E-07	-	1.10E-08	-
20	Ca	2.29E-06	2.00E-08	1.20E-08	2.29E-06	2.35E-06	-	4.1E-10	-
21	Sc	1.48E-09	1.00E-20	1.00E-20	1.22E-09	1.16E-09	-	1.00E-20	-
22	Ti	1.05E-07	5.80E-10	1.00E-20	8.60E-08	9.00E-08	-	5.80E-10	-
23	V	1.00E-08	1.00E-10	1.00E-20	1.05E-08	9.50E-09	-	1.00E-10	-
24	Cr	4.68E-07	1.00E-08	1.00E-20	4.84E-07	4.80E-07	-	1.00E-08	-
25	Mn	2.88E-07	2.3E-08	1.00E-20	3.42E-07	3.50E-07	-	2.30E-08	-
26	Fe	2.82E-05	3.0E-06	5.00E-07	4.68E-05	3.38E-05	-	6.31E-07	3.24E-05
27	Co	8.32E-08	1.00E-20	1.00E-20	2.24E-09	8.27E-08	-	1.00E-09	-
28	Ni	1.78E-06	1.00E-07	1.80E-08	1.76E-06	1.80E-06	-	1.82E-08	-
29	Cu	1.62E-08	1.50E-09	1.00E-20	1.87E-08	2.00E-08	-	1.50E-09	-
30	Zn	3.98E-08	2.00E-08	1.00E-20	4.52E-08	4.70E-08	-	2.00E-08	-

Table A.1: Pre-defined abundances sets.

There is limited control over the abundance of dust with respect to the gaseous component and usuallythe dust-to-gas ratio will remain constant. The keyword `function sublimation` however will turn on a predefined grain abundance function that mimics the effects of dust sublimation, steeply decreasing the grain abundance when the temperature is above the sublimation temperature for a specific grain size bin. The function that is used is as follows:

$$A_g = \exp\left[-\left(\frac{T_g}{T_{sub}}\right)^3\right] \tag{A.1}$$

where T_g is the grain temperature and T_{sub} is the sublimation temperature. This command is particularly helpful when dealing with regions close to the luminosity source, such as the inner boundary of the torus.

Bibliography

Allende Prieto, C., Lambert, D. L., & Asplund, M. 2001, ApJ, 556, L63

—. 2002, ApJ, 573, L137

Aller, L. H., & Czyzak, S. J. 1983, ApJS, 51, 211

Antonucci, R. 1993, ARA&A, 31, 473

Antonucci, R. R. J., & Miller, J. S. 1985, ApJ, 297, 621

Bacon, R., Adam, G., Baranne, A., et al. 1995, A&AS, 113, 347

Baldwin, J. A., Ferland, G. J., Martin, P. G., et al. 1991, ApJ, 374, 580

Baldwin, J. A., Phillips, M. M., & Terlevich, R. 1981, PASP, 93, 5

Barden, S. C., & Wade, R. A. 1988, in Astronomical Society of the Pacific Conference Series, Vol. 3, Fiber Optics in Astronomy, ed. S. C. Barden, 113–124

Barvainis, R. 1987, ApJ, 320, 537

Beckert, T., & Duschl, W. J. 2004, A&A, 426, 445

Beckmann, V., & Shrader, C. R. 2012, Active Galactic Nuclei (Wiley-vch)

Bentz, M. C., Denney, K. D., Grier, C. J., et al. 2013, ApJ, 767, 149

Berkhuijsen, E. M., & Fletcher, A. 2015, MNRAS, 448, 2469

Binette, L., Wilson, A. S., & Storchi-Bergmann, T. 1996, A&A, 312, 365

Boroson, T. A., & Green, R. F. 1992, ApJS, 80, 109

Burtscher, L., Meisenheimer, K., Tristram, K. R. W., et al. 2013, A&A, 558, A149

Cameron, A. G. W. 1982, in Essays in Nuclear Astrophysics, ed. C. A. Barnes, D. D. Clayton, & D. N. Schramm

Ciroi, S., Afanasiev, V. L., Moiseev, A. V., et al. 2005, MNRAS, 360, 253

Ciroi, S., Contini, M., Rafanelli, P., & Richter, G. M. 2003, A&A, 400, 859

Coles, P., & Jones, B. 1991, MNRAS, 248, 1

Collin, S., & Zahn, J.-P. 1999, A&A, 344, 433

—. 2008, A&A, 477, 419

Congiu, E., Berton, M., Giroletti, M., et al. 2017a, A&A, 603, A32

Congiu, E., Contini, M., Ciroi, S., et al. 2017b, ArXiv e-prints, arXiv:1710.01173

—. 2017c, MNRAS, 471, 562

Content, R. 1997, in Proc. SPIE, Vol. 2871, Optical Telescopes of Today and Tomorrow, ed. A. L. Ardeberg, 1295–1305

Contini, M., & Aldrovandi, S. M. V. 1983, A&A, 127, 15

Contini, M., Cracco, V., Ciroi, S., & La Mura, G. 2012, A&A, 545, A72

Contini, M., Rodríguez-Ardila, A., & Viegas, S. M. 2003, A&A, 408, 101

Cowie, L. L., & Songaila, A. 1986, ARA&A, 24, 499

Cracco, V., Ciroi, S., di Mille, F., et al. 2011, MNRAS, 418, 2630

Elitzur, M., & Shlosman, I. 2006, ApJ, 648, L101

Elvis, M., Wilkes, B. J., McDowell, J. C., et al. 1994, ApJS, 95, 1

Emmering, R. T., Blandford, R. D., & Shlosman, I. 1992, ApJ, 385, 460

Evans, I. N., Tsvetanov, Z., Kriss, G. A., et al. 1993, ApJ, 417, 82

Fanaroff, B. L., & Riley, J. M. 1974, MNRAS, 167, 31P

Feldmeier, J. J., Brandt, W. N., Elvis, M., et al. 1999, ApJ, 510, 167

Ferland, G. J., & Shields, G. A. 1978, ApJ, 226, 172

Ferland, G. J., Porter, R. L., van Hoof, P. A. M., et al. 2013, RMxAA, 49, 137

Fischer, T. C., Crenshaw, D. M., Kraemer, S. B., & Schmitt, H. R. 2013, ApJS, 209, 1

Francis, P. J. 1993, ApJ, 407, 519

Fritz, J., Franceschini, A., & Hatziminaoglou, E. 2006, MNRAS, 366, 767

Ghisellini, G. 2010, in American Institute of Physics Conference Series, Vol. 1242, American Institute of Physics Conference Series, ed. G. Bertin, F. de Luca, G. Lodato, R. Pozzoli, & M. Romé, 43–54

Giommi, P., Padovani, P., Polenta, G., et al. 2012, MNRAS, 420, 2899

Glass, I. S. 1992, MNRAS, 256, 23P

Goodrich, R. W. 1989, ApJ, 342, 224

Granato, G. L., Danese, L., & Franceschini, A. 1997, ApJ, 486, 147

Grevesse, N., & Sauval, A. J. 1998, Space Sci. Rev., 85, 161

Grupe, D. 2000, New A Rev., 44, 455

Guainazzi, M., Risaliti, G., Awaki, H., et al. 2016, MNRAS, 460, 1954

Heckman, T. M., & Best, P. N. 2014, ARA&A, 52, 589

Ho, L. C. 2008, ARA&A, 46, 475

Holweger, H. 2001, in Joint SOHO/ACE workshop "Solar and Galactic Composition"

Hönig, S. F., & Beckert, T. 2007, MNRAS, 380, 1172

Hönig, S. F., & Kishimoto, M. 2010, A&A, 523, A27

Kaspi, S., Smith, P. S., Netzer, H., et al. 2000, ApJ, 533, 631

Kauffmann, G., Heckman, T. M., Tremonti, C., et al. 2003, MNRAS, 346, 1055

Kewley, L. J., Dopita, M. A., Sutherland, R. S., Heisler, C. A., & Trevena, J. 2001, ApJ, 556, 121

Kewley, L. J., Groves, B., Kauffmann, G., & Heckman, T. 2006, MNRAS, 372, 961

Khromov, G. S. 1989, Space Sci. Rev., 51, 339

Komossa, S., & Schulz, H. 1997, A&A, 323, 31

Koshida, S., Minezaki, T., Yoshii, Y., et al. 2014, ApJ, 788, 159

Kraemer, S. B., Schmitt, H. R., & Crenshaw, D. M. 2008, ApJ, 679, 1128

Kreimeyer, K., & Veilleux, S. 2013, ApJ, 772, L11

Krolik, J. H. 2007, ApJ, 661, 52

Krolik, J. H., & Begelman, M. C. 1986, ApJ, 308, L55

—. 1988, ApJ, 329, 702

Laing, R. A., Jenkins, C. R., Wall, J. V., & Unger, S. W. 1994, in Astronomical Society of the Pacific Conference Series, Vol. 54, The Physics of Active Galaxies, ed. G. V. Bicknell, M. A. Dopita, & P. J. Quinn, 201

Leroy, A. K., Hughes, A., Schruba, A., et al. 2016, ApJ, 831, 16

Madau, P. 1988, ApJ, 327, 116

Maksym, W. P., Fabbiano, G., Elvis, M., et al. 2016, ApJ, 829, 46

Marinucci, A., Bianchi, S., Nicastro, F., Matt, G., & Goulding, A. D. 2012, ApJ, 748, 130

Mathis, J. S., Rumpl, W., & Nordsieck, K. H. 1977, ApJ, 217, 425

Mathur, S. 2000, MNRAS, 314, L17

Meaburn, J., Whitehead, M. J., & Pedlar, A. 1989, MNRAS, 241, 1P

Meyer, D. M., Jura, M., & Cardelli, J. A. 1998, ApJ, 493, 222

Mor, R., Netzer, H., & Elitzur, M. 2009, ApJ, 705, 298

Morisset, C. 2013, pyCloudy: Tools to manage astronomical Cloudy photoionization code, Astrophysics Source Code Library, ascl:1304.020

Morse, J. A., Cecil, G., Wilson, A. S., & Tsvetanov, Z. I. 1998, ApJ, 505, 159

Mulchaey, J. S., Wilson, A. S., & Tsvetanov, Z. 1996, ApJS, 102, 309

Müller-Sánchez, F., Prieto, M. A., Hicks, E. K. S., et al. 2011, ApJ, 739, 69

Mullman, K. L., Lawler, J. E., Zsargó, J., & Federman, S. R. 1998, ApJ, 500, 1064

Nakanishi, H., & Sofue, Y. 2016, PASJ, 68, 5

Nenkova, M., Sirocky, M. M., Ivezić, Ž., & Elitzur, M. 2008a, ApJ, 685, 147

Nenkova, M., Sirocky, M. M., Nikutta, R., Ivezić, Ž., & Elitzur, M. 2008b, ApJ, 685, 160

Netzer, H. 2008, New A Rev., 52, 257

—. 2015, ARA&A, 53, 365

O'Dea, C. P., Baum, S. A., & Stanghellini, C. 1991, ApJ, 380, 66

Osterbrock, D. E. 1981, ApJ, 249, 462

Osterbrock, D. E., & Ferland, G. J. 2006, Astrophysics of gaseous nebulae and active galactic nuclei (University Science Books)

Osterbrock, D. E., & Pogge, R. W. 1985, ApJ, 297, 166

—. 1987, ApJ, 323, 108

Osterbrock, D. E., Tran, H. D., & Veilleux, S. 1992, ApJ, 389, 305

Padovani, P. 2016, A&A Rev., 24, 13

Padovani, P., & Giommi, P. 1995, ApJ, 444, 567

Padovani, P., Alexander, D. M., Assef, R. J., et al. 2017, A&A Rev., 25, 2

Panessa, F., & Bassani, L. 2002, A&A, 394, 435

Pequignot, D., & Dennefeld, M. 1983, A&A, 120, 249

Pier, E. A., & Krolik, J. H. 1992, ApJ, 401, 99

Pogge, R. W. 1988, ApJ, 328, 519

—. 1989, ApJ, 345, 730

Robinson, A., Vila-Vilaro, B., Axon, D. J., et al. 1994, A&A, 291, 351

Rodríguez-Ardila, A., Contini, M., & Viegas, S. M. 2005, MNRAS, 357, 220

Rubin, R. H., Dufour, R. J., & Walter, D. K. 1993, ApJ, 413, 242

Rubin, R. H., Simpson, J. P., Haas, M. R., & Erickson, E. F. 1991, ApJ, 374, 564

Salz, M., Banerjee, R., Mignone, A., et al. 2015, A&A, 576, A21

Savage, B. D., & Sembach, K. R. 1996, ARA&A, 34, 279

Schartmann, M., Burkert, A., Krause, M., et al. 2010, MNRAS, 403, 1801

Schartmann, M., Meisenheimer, K., Camenzind, M., Wolf, S., & Henning, T. 2005, A&A, 437, 861

Schmitt, H. R., Donley, J. L., Antonucci, R. R. J., Hutchings, J. B., & Kinney, A. L. 2003, ApJS, 148, 327

Seyfert, C. K. 1943, ApJ, 97, 28

Shi, Y., Rieke, G. H., Smith, P., et al. 2010, ApJ, 714, 115

Siebenmorgen, R., Heymann, F., & Efstathiou, A. 2015, A&A, 583, A120

Snow, T. P., Destree, J. D., & Jensen, A. G. 2007, ApJ, 655, 285

Stalevski, M., Fritz, J., Baes, M., Nakos, T., & Popović, L. Č. 2012, MNRAS, 420, 2756

Stasińska, G. 1984, A&A, 135, 341

Suganuma, M., Yoshii, Y., Kobayashi, Y., et al. 2006, ApJ, 639, 46

Sulentic, J. W., Marziani, P., Zamanov, R., et al. 2002, ApJ, 566, L71

Tadhunter, C., & Tsvetanov, Z. 1989, Nature, 341, 422

Tadhunter, C. N., Fosbury, R. A. E., di Serego Alighieri, S., et al. 1988, MNRAS, 235, 403

Tran, H. D. 2003, ApJ, 583, 632

Tristram, K. R. W., Meisenheimer, K., Jaffe, W., et al. 2007, A&A, 474, 837

Tristram, K. R. W., Raban, D., Meisenheimer, K., et al. 2009, A&A, 502, 67

Tsvetanov, Z. I., Kriss, G. A., & Ford, H. C. 1996, Vistas in Astronomy, 40, 71

Unger, S. W., Pedlar, A., Axon, D. J., et al. 1987, MNRAS, 228, 671

Urry, C. M., & Padovani, P. 1995, PASP, 107, 803

Veilleux, S., & Osterbrock, D. E. 1987, ApJS, 63, 295

Viegas, S. M., & Contini, M. 1994, ApJ, 428, 113

Viegas-Aldrovandi, S. M., & Contini, M. 1989, A&A, 215, 253

Vollmer, B., Beckert, T., & Davies, R. I. 2008, A&A, 491, 441

Wada, K., Papadopoulos, P. P., & Spaans, M. 2009a, ApJ, 702, 63

—. 2009b, ApJ, 702, 63

Wang, J., Fu, J., Aumer, M., et al. 2014, MNRAS, 441, 2159

Weymann, R. J., Carswell, R. F., & Smith, M. G. 1981, ARA&A, 19, 41

Yoshida, M., Yagi, M., Okamura, S., et al. 2002, ApJ, 567, 118

Zamorani, G., Henry, J. P., Maccacaro, T., et al. 1981, ApJ, 245, 357